Chapter 4
The Measurement of Oceanic Ambient Noise

Introduction

Ambient noise investigations constitute one of the largest sections of the Journal of the Acoustical Society of America. Urick (1984) has summarized a good many of these experimental papers and his report is valuable as it updates and extends the work of Wenz (1972). In this chapter the discussion focuses on the key aspects of ambient noise by interpreting the experimental observations in light of the fundamental production mechanisms of ambient noise. The theoretical treatments of these source mechanisms can be found in Chapter 3, with the appendices containing detailed derivations. The source mechanisms are used in this chapter as part of our overview of the characteristics of measured ambient noise. Since the measurements span some 60 years, the following question arises: What was measured and how do these measurements compare with those currently performed?

Repeatable and accurate measurement of the noise background requires high-quality calibrated receivers. Calibrated hydrophones were not available prior to World War II; consequently, the ambient noise measurements discussed in this treatment were made during and after that war. In his history of underwater acoustics, Goodman (2004) points out that although magnetostriction and piezoelectricity were discovered in the nineteenth century, additional hydrophone technology development was required to convert acoustic pressures to amplified voltages that enabled the practical application of these electromechanical phenomena. The conductive and corrosive nature of sea water as well as the requirement to operate over a wide range of depths and pressures were additional technological difficulties to be overcome. Langevin, Chilowsky, and Fessenden produced transmitters capable of echo-ranging to a distance of miles. Fessenden used a moving coil transmitter. Langevin developed a resonant quartz receiver that was replaced by the unstable Rochelle salt and ammonium dihydrogen phosphate. Between 1940 and 1950, barium titanate piezoelectric ceramics replaced these in hydrophone applications. By the mid-1950s, two types of receivers were used: (1) moving-coil, oil-filled, omnidirectional hydrophones, and (2) the barium titanate hydrophones with a relatively flat response to the kilohertz region. The availability of hydrophones capable of operating in the ocean environment, even with primitive data acquisition and analysis systems, provided the technological tools necessary for oceanic ambient

noise research. The further development of lead zirconate titanate enabled the development of wide-band sensitive hydrophones, which are widely used by investigators in the study of oceanic noise.

The first section of this chapter provides an overview of a measurement system that spans the evolution of technology to provide the basis for interpreting and comparing measured results from the war years to the present. The treatment is general but specific to the determination of the mean square pressure, the pressure spectral density, the correlation function, and other noise characteristics. The current acoustic definitions and conventions used in this chapter along with these quantities are found in Appendix B, where the American National Standards are discussed and applied. The second portion of this chapter is a phenomenological overview of ambient noise from the characteristic of Wenz (1962) to the present using selected references of noise studies.

Noise Measurement

The measurement of ambient noise has progressed from analog measurement to digitization and digital fast Fourier transform (FFT) analyses. Early measurements focused on the root mean square pressure, p_{rms}, mean square pressure $< p^2 >$, or the autocorrelation function, $\Gamma_p(\tau)$, in the specified band. A representative measurement schematic is shown in Fig. 4.1. The calibrated hydrophone converts the pressure fluctuations in the water to charge fluctuations, a charge-sensitive amplifier converts the signal to a time-varying voltage, and this temporal voltage variation is band-pass-filtered. The implementation of the filter was often the application scheme whereby the voltage was multiplied by $\cos(2\pi f_o t)$ and $\sin(2\pi f_o t)$. Since these quantities are orthogonal to one another at any time t, the cross-products integrate to zero and for all practical purposes can be treated as independent variables, with two degrees of freedom. The square of the voltage $v_o^2(t)$ is integrated over a time interval, T, for which conditions were considered stationary as determined by the correlative properties and the state of the sea. The output of this integration is then sampled and summed to provide an estimate of the mean square voltage $\langle v_o^2 \rangle$.
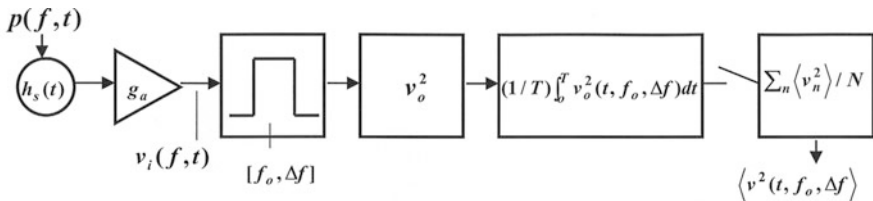

Fig. 4.1 A noise measurement system schematic that illustrates the measurement of mean square ambient noise pressures. This schematic can be applied to both analog and fast Fourier transform systems

It is readily seen by analogy that the estimate of the mean square voltage or mean square pressure in this single band Δf wide is equivalent to the complex product of FFTs, $P(f) \cdot P(f)^*$, of the pressure signal. However, sound that is continuous-bounded, nonperiodic, and stationary poses a problem for Fourier analysis. Fourier integrals are infinite integrals and consequently convergence must be considered. The continuous version of Parseval's theorem, Plancherel's theorem (see Middleton (1987, p 137), Appendix B),

$$\int_{-\infty}^{+\infty} |p(t)|^2 dt = 2\pi \cdot \int_{-\infty}^{+\infty} P(\omega) \cdot P(\omega)^* d\omega = \int_{-\infty}^{+\infty} P(f) \cdot P(f)^* df, \quad (1)$$

states the problem. If the integral of $|p(t)|^2$ converges, then the integral of $|P(f)|^2$ converges. If the pressure variation is random but stationary, $|p(t)|^2$ does not diminish as $t \to \infty$ and the integral will not converge. However, if we restrict p(t) such that

$$\begin{array}{ll} p(t) = 0, & -\infty < t < -T/2 \; ; \; T/2 < t < +\infty \\ p(t) \neq 0, & -T/2 < t < +T/2 \end{array}, \quad (2)$$

then for large but finite T

$$\int_{-\infty}^{+\infty} |p(t)|^2 dt \to \int_{-T/2}^{+T/2} |p(t)|^2 dt = T<p(t)^2>_T = 2\pi \int_{-\infty}^{+\infty} |P(\omega)|^2 d\omega$$
$$= \int_{-\infty}^{+\infty} |P(f)|^2 df \quad (3)$$

where $P(f) = \int_{-T/2}^{+T/2} p(t) exp(-i2\pi f t) dt$.

These integrals decrease at a sufficient rate with $\omega = 2\pi f \to \infty$ to ensure convergence for large but not infinite values of T:

$$< p(t)^2>_T = [2\pi/T]\int_{-\infty}^{+\infty} |P(\omega)|^2/d\omega = [1/T]\int_{-\infty}^{+\infty} |P(f)|^2 df$$
$$< p(t)^2>_T/2\pi = \int_{-\infty}^{+\infty} (|P(\omega)|^2/T) d\omega \; and \; < p(t)^2>_T = \int_{-\infty}^{+\infty} (|P(f)|^2/T) df$$
$$(|P(\omega)|^2/T) \; and \; (|P(f)|^2/T) \; are \; spectral \; densities \; per \; unit \; time.$$
$$(4)$$

For this case of bounded, nonperiodic, and stationary pressure fluctuations, one can define time-varying means and mean square quantities for large T:

$$< p(t)>_T = (1/T) \int_{-T/2}^{+T/2} p(t) dt \; and \; < p(t)^2>_T = \int_{-\infty}^{+\infty} (|P(f)|^2/T) df. \quad (5)$$

The Autocorrelation Function, $\Gamma_p(\tau)$

The variation with time can be described by use of the autocorrelation function:

$$
\begin{aligned}
\Gamma_p(\tau) &\equiv \underset{T\to\infty}{Lim}\left[(1/T)\int_{-T/2}^{+T/2} p(t)p(t+\tau)dt\right]; \\
&\to \Gamma_p(0) \equiv \underset{T\to\infty}{Lim}\left[(1/T)\int_{-T/2}^{+T/2} p(t)^2 dt\right] = <p(t)^2>_T.
\end{aligned}
\tag{6}
$$

The ensemble-averaged mean square value of $<p(t)>_T$ can be determined by the following product:

$$
\ll p(t) >_T^2 >_e = < (1/T)\int_{-T/2}^{T/2} p(t_1)dt_1\,(1/T)\int_{-T/2}^{T/2} p(t_2)dt_2 >_e.
\tag{7}
$$

The autocorrelation function can be related to this quantity:

$$
\ll p(t) >_T^2 >_e = (1/T^2)\int_{-T/2}^{T/2}\cdot\int_{-T/2}^{T/2}\Gamma_p(t_2-t_1)dt_2 dt_1 \to (2/T)\int_0^T (1-\tau/T)\Gamma_p(\tau)d\tau.
\tag{8}
$$

The Fourier transform of the autocorrelation function is $2\pi/T$ times the spectral density $|P(\omega)|^2$ of p(t):

$$
F\{\Gamma_p(\tau)\} = (1/2\pi)\int_{-\infty}^{+\infty}\Gamma_p(\tau)exp(-i\omega\tau)d\tau \to 2\pi P(\omega)P(\omega)^*/T.
\tag{9}
$$

The Power Spectral Density

Continuing with measurement of stationary but random pressure fluctuations, one needs to consider sampling. Each observed time series of p(t) is one member, a sample member of the family of all possibilities, of the ensemble. Let the ensemble be represented by {p(t)} and let $p^j(t)$ be the jth sample of the random process {p(t)}. If the variations of the mean, mean square, and autocorrelation of p(t) exhibit significant variation with time, the process is nonstationary, if there are no significant variations with time, the process is weakly stationary, and if all moments of p(t) show no variation with time, the process is strongly stationary or stationary in the strict sense. If a member of a stationary process is representative of the whole ensemble, then the process can be considered ergodic.

For $p^j(t)$, which vanishes everywhere outside the interval $t_1 - T/2 < t < t_1 + T/2$, the average power, $<\Pi(T)>$, or average energy, $<E(T)>$, has no dependence on t over the interval and we have

$$\Pi^j(T) \equiv E^j(T)/T = (1/T) \int_{t_1-T/2}^{t_1+T/2} p^j(t)^2 dt. \tag{10}$$

According to Parseval's theorem,

$$\Pi^j(T) \equiv E^j(T)/T = \int_{-\infty}^{+\infty} \{|P^j(f)|^2/T\} df. \tag{11}$$

$$W_p^j(f)_T \equiv 2|P^j(f)_T|^2/T \;\rightarrow\; \Pi^j(T) = \int_o^\infty W_p^j(f)_T df. \tag{12}$$

Since the power spectral density, $W_p^j(f)_T$, is an even function of f, one does not need the negative frequencies and the factor of 2 in the definition above accounts for the change in the integration limits.

One can then define a linear average power as

$$< \Pi(T)>_{NT} = 1/N \sum_{j=1}^N \Pi^j(T) = 1/N \sum_{j=1}^N \int_o^\infty W_p^j(f)_T df. \tag{13}$$

If the process is ergodic, one can perform an ensemble average to obtain

$$< \Pi(T)>_e = < \Pi^j(T)>_e = \int_o^\infty < W_p^j(f)_T>_e df = \int_o^\infty W_p(f)_T df. \tag{14}$$

For an ergodic processes, the temporal average and expectation are equal,

$$<\Pi(T)>_{NT} = <\Pi(T)>_e. \tag{15}$$

The expected value of the power spectral density, as a direct consequence of the Wiener–Khintchine theorem (Middleton 1987), is related to the covariance function, K, and using Eq. (12),

$$\begin{aligned} W_p(f)_T &= 2\,F\{K\} = 2 \int_{-\infty}^{+\infty} K \exp(-i\omega t) dt \\ &= < (2/T)|F(p(T))|^2>_e \end{aligned}. \tag{16}$$

The Fourier transform of the autocorrelation or covariance function is equal to 2/T times the spectral densities. Thus, the autocorrelation and covariance are equal to the inverse transform of the power spectral density.

$$\begin{aligned} W_p(f)_T &= <(2/T)|F(p(T)|^2>_e = <F\{\Gamma(\tau)\}>_e \\ &\rightarrow <\Gamma(\tau)>_e = (1/2) \int_{-\infty}^{+\infty} W_p(f)_T \exp(+i\omega \tau) df = K(\tau). \end{aligned} \tag{17}$$

The response of measurement system shown in Fig. 4.1 to stationary statistical noise can be summarized by the power spectral density in relationship to the Fourier transforms of the autocorrelation, covariance, or pressure.

$$W(f)_T = <F\{\Gamma(\tau)\}>_e = <F\{K(\tau)\}>_e$$
$$= 2\pi <P(\omega)P(\omega)^*>/T = <P(f)P(f)^*>/T. \tag{18}$$

The power spectral density level should be referenced to watts per square meter hertz as the natural units or when the power per unit area is proportional to pressure squared, the reference quantity is micropascals squared per hertz. The power spectral density level is defined as follows:

$$\text{Power spectral density} \equiv 10 \cdot \log_{10}[W(f)_T/W_{ref}(f)_T]$$
$$= 10 \cdot \log_{10}[(<p^2(t)>_T/\Delta f)/((\mu Pa)^2/Hz)] \; ; \; dB \, re \, (\mu Pa)^2/Hz). \tag{19}$$

Some Simple Statistical Concepts

The texts *Detection of Signals in Noise* by Whalen (1971) and *Measurement and Analysis of Random Data* by Bendat and Piersol (1966) are excellent in their treatment of the ocean acoustics measurement problem. Although it is realistic to state that deterministic, transient, and random data analysis is an all-inclusive subject, it is the purpose here to simplify the treatment to the direct application of some simple statistics applied to ambient noise measurements. One needs to distinguish between time averages and ensemble averages, because they are only equivalent in the case of wide-sense stationary processes.

The simplest noise case is a stationary pressure time series that has a white spectral density, uniform with frequency, and is a zero mean Gaussian random process. As shown in Fig. 4.1, the time-varying pressure is converted to a time-varying voltage by the hydrophone and preamplifier, $p(f, t) \rightarrow v_i(f, t)$. The pressure is a zero mean Gaussian process and, likewise, so is the voltage, with the following probability distribution:

$$p_d(v_i) = \exp(-v_i^2/2\sigma^2)/\sigma\sqrt{2\pi}. \tag{20}$$

The voltage, $v_i(f, t)$, a Gaussian random variable, is filtered by a linear filter with a center frequency, $2\pi f_o = \omega_o$, and bandwidth $\Delta f[Hz]$. The linear filter output, $v_o(f_o, \Delta f, t)$, is a narrow-band Gaussian variable and when viewed on an oscilloscope is a slowly undulating cosinusoidal function of time:

$$v_o(f_o, \Delta f, t) = v_{oi}(f_o, \Delta f, t)\cos(\omega_o t + \phi(t))$$
$$= (v_{oi}\cos(\phi(t))\cos(\omega_o t) + (-v_{oi}\sin(\phi(t)))\sin(\omega_o t) \tag{21}$$
$$= \alpha(t)\cos(\omega_o t) + \beta(t)\sin(\omega_o t)$$

Since the sine and cosine are orthogonal or in quadrature, and since α and β are Gaussian variables, one usually treats these quantities as independent even though over short-time samples there is a phase for which they will be correlated. Consequently, the quantities are strictly not statistically independent random variables. However, the correlation of large numbers of sine and cosine samples

decreases in inverse proportion to the number of samples and thus can be treated as statistically independent.

The voltage when squared and integrated over time T is

$$
\begin{aligned}
< v^2 >_T &= (1/T)\int_o^T v_o^2 dt = (1/T)\int_o^T (\alpha(t)^2 \cos(\omega_o t)^2 + \beta(t)^2 \sin(\omega_o t)^2)dt \\
&= (1/T)\alpha(t)^2 \int_o^t \cos(\omega_o t)^2 dt + (1/T)\beta(t)^2 \int_o^t \sin(\omega_o t)^2 dt \\
&= (1/2)\cdot(\alpha(t)^2 + \beta(t)^2).
\end{aligned}
\tag{22}
$$

In the above equation, cross-product terms integrated to zero. Here it has been assumed that the temporal variation of the Gaussian variables α and β is slow compared with the period of the filter's center frequencies and the integration variable T. With the introduction of a new variable $z^2 = 2 < v^2 >_T = \alpha^2 + \beta^2$, the probability density can be determined by standard techniques. Given that α and β are Gaussian,

$$
\begin{aligned}
p_d(\alpha) &= (1/\sigma\sqrt{2\pi})\exp(-\alpha^2/2\sigma^2) \quad and \quad p_d(\beta) = (1/\sigma\sqrt{2\pi})\exp(-\beta^2/2\sigma^2) \\
p_d(\alpha,\beta) &= p_d(\alpha)\cdot p_d(\beta) = (1/2\pi\sigma^2)\exp(-(\alpha^2+\beta^2)/2\sigma^2)
\end{aligned}
\tag{23}
$$

To determine the probability distribution for the amplitude z and its square z^2, one uses the cumulative distribution function, P_c. If α and β are statistically independent random variables, the joint cumulative distribution function is

$$
P_c(z \le Z) = \iint p_d(\alpha,\beta)d\alpha\,d\beta.
\tag{24}
$$

With a change of variables, $\alpha = z\cos(\theta)$, $\beta = z\sin(\theta)$, with $z = (\alpha^2 + \beta^2)^{1/2}$ and $\theta = tan^{-1}(\beta/\alpha)$, the Jacobian of the transformation is $|J| = z$. The result is the joint cumulative function

$$
P_c(z \le Z) = \iint p_d(\alpha = z\cos(\theta))p_d(\beta = z\sin(\theta))\,|J|dzd\theta.
\tag{25}
$$

Substitution of the probability density functions and integration over θ yields

$$
\begin{aligned}
P_c(z \le Z) &= \int_o^Z \cdot \int_o^{2\pi} (1/2\pi\sigma^2)exp(-z^2/2\sigma^2)zdzd\theta \\
&= \int_o^Z \cdot(1/\sigma^2)exp(-z^2/2\sigma^2)zdz.
\end{aligned}
\tag{26}
$$

Differentiation of this expression produces the probability density of the magnitude z or the envelope:

$$
p_d(Z) = (dP_c(z < Z)/dZ) = (Z/\sigma^2)exp(-Z^2/2\sigma^2), \ Z \ge 0.
\tag{27}
$$

The above probability distribution of the envelope or the root mean square voltage is recognized as the Rayleigh distribution. This distribution has an expected mean value, $E[z] = (\pi/2)^{1/2}\sigma$, and an expected second moment, $E[z^2] = 2\sigma^2$.

The procedure can be repeated to determine the probability distribution for the squared variable, z^2. First, let $u = z^2$ and use the fact $P_c(u \leq Z^2 = U) = P_c(z \leq Z)$.

$$
\begin{aligned}
P_c(z \leq Z) &= \int_o^Z [(z/\sigma^2) exp(-z^2/2\sigma^2)]dz \\
&= \int_o^{Z^2} [(1/2\sigma^2) exp(-z^2/2\sigma^2)]dz^2.
\end{aligned}
\tag{28}
$$

In terms of the variable u,

$$
\begin{aligned}
P_c(u \leq U) &= \int_o^{Z^2} [(1/2\sigma^2) exp(-z^2/2\sigma^2)]dz^2 \\
&= \int_o^U [(1/2\sigma^2) exp(-u/2\sigma^2)]du.
\end{aligned}
\tag{29}
$$

Differentiation of the cumulative distribution function yields

$$
p(U = Z^2) = dP_c(u \leq U)/dU = (1/2\sigma^2)\, exp\,(-U/2\sigma^2).
\tag{30}
$$

This probability density can be written as follows:

$$
p_d(z^2) = (1/2\sigma^2)\, exp\,(-z^2/2\sigma^2)\,, E[z^2] = 2\sigma^2\,,\; E[z^4] = 4\sigma^4.
\tag{31}
$$

This is an exponential distribution or a two degrees of freedom χ^2 distribution. Thus, the description of the noise-processing scheme is complete. The postsummation of N independently sampled noise estimates is also χ^2 distributed with 2N degrees of freedom since the sum of χ^2 variables is also χ^2.

Phenomenological Observations

In *Ambient Noise in the Sea*, Urick (1984) commented on the prolific nature of the literature concerning theories of sound generation at the sea surface and measurements of the temporal and spatial spectral characteristics. The idealized spectral characteristic suggested by Urick was in agreement with the schematic of Wenz (1962) and for frequencies greater than 500 Hz is consistent with the observations of Knudsen et al. (1948) and Wenz's "rule of fives." The deepwater noise spectrum level can be described by

$$
\begin{aligned}
&NL(f, U) = 25 - 10 \cdot log[f^{5/3}] + 10 \cdot log[(U/5)^{5/3} \\
&or \\
&NL(f, U) = 25 - (5/3) \cdot 10 \cdot [log[f] - log[U/5]]
\end{aligned}
\tag{32}
$$

where f is the frequency (kHz), U is the wind speed (knots), and NL is the noise level, which at 1 kHz and 5-knot wind speed is 25 dB re (20 μN/m^2)^2/Hz. He recommended the addition of another 5 dB for shallow water levels. Wenz observed in the 10–500-Hz band that the measured noise levels were often variable, dominated

by shipping noise, with only weak wind-speed dependence. The shape of the spectrum also was found to vary from a positive slope to a steep negative slope. Below 10 Hz, he indicated a steep spectral slope of up to 10 dB/octave as the frequency decreased. These trends are shown in Fig. 4.2. Also shown in this figure are limits based on lake noise measurements, heavy rain, and the thermal noise limit due to molecular agitation. It is convenient to discuss this spectrum in nominal frequency
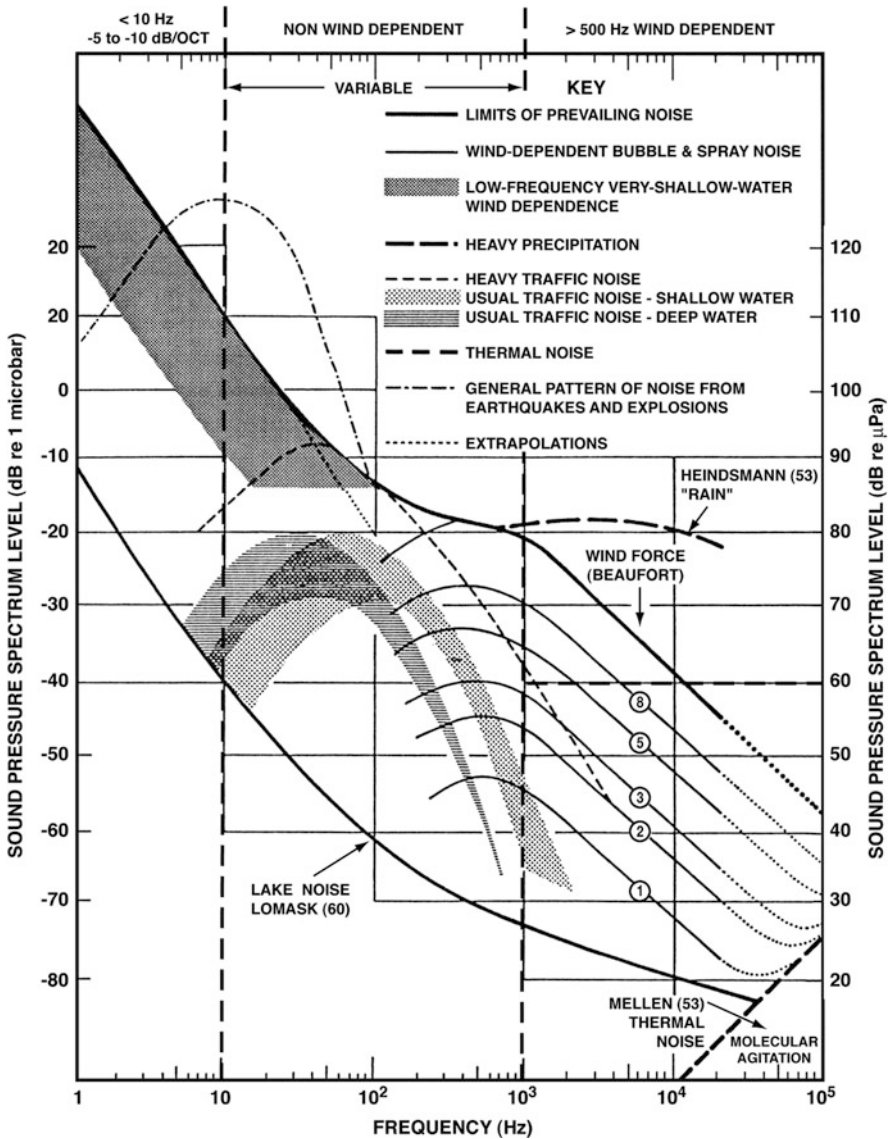

Fig. 4.2 The Wenz curves for ambient noise spectrum levels [adapted from Wenz (1962)]

regions. For example, the frequency region below 20 Hz is referred to as infrasonic; the band between 20 and 20 kHz is the sonic region; and that greater than 20 kHz is the ultrasonic region.

Infrasonic Noise

Infrasonic noise (f ≤ 20 Hz) was thought to be due to wave–wave interactions, capillary wave interactions, wave–turbulence interactions, and atmospheric turbulence. The results of several investigations since the time of Wenz are shown in Fig. 4.3. The general trend observed in the measured results is a decrease with frequency, 0.2–5 Hz, of the noise spectrum level of 5–12 dB/octave, dependent on the wind speed. These infrasonic experiments were difficult to conduct and temperature fluctuations and local flow noise can affect the measurement sensors. In addition, knowledge of a wide area of the bottom and the sea surface spectrum is required to define the experimental conditions. In general, the results shown in Fig. 4.3 agree qualitatively with the formulation of Miche (1944) and the further treatments by Longuet-Higgins (1950) insofar as the spectral peak is approximately double that of the surface wave spectrum and correlated with the surface displacement spectrum.

Other candidates for the production of the spectrum characteristics were the turbulent boundary pressure fluctuations, wave–turbulence interactions, and capillary wave interactions. Yen and Perrone (1974) and Goncharov (1970) placed estimates on these mechanisms and showed that below 5 Hz the estimated magnitude and spectral character are inconsistent with the observations, whereas above 5 Hz they provide a lower limit on the noise observed. The estimates of the wave–wave interaction by Hughes (1976) and Brekhovskikh (1966) appear to be consistent with the experimental results.

The measurements shown in Fig. 4.3, were complied by Kibblewhite and Evans (1985) and show that wave–wave interaction can the characteristic of the ambient noise spectrum at frequencies less than 5 Hz and the presence of the microseismic spectral peak in the 0.2 Hz. However, a definitive experiment that employs simultaneous measurement with seismic sensors, very low-frequency pressure sensors and wave spectrum instrumentation has yet to be performed. The work of Kibblewhite in extending the Wenz curve to the infrasonic region, although meritorious and timely, should be reexamined.

Cato (1991) extended the wave interaction theory and compared calculations with the results obtained from careful experiments in the lake of the Woronora Dam. Measurements in the 35-m-deep lake showed the expected agreement between the wave height spectrum and the noise spectrum. As a basis for comparison, Cato used a formulation of the wave–wave interaction using the Heaviside function to specify the sea surface boundary condition. This theoretical method is equivalent to the use of retarded Green's functions, as discussed in Chapter 3. The measured noise levels were higher than the open-ocean levels; however, the agreement with theoretical expectations for the specific conditions in his experiment was found to be significant. By extrapolation of these results, Cato concluded that there was no longer
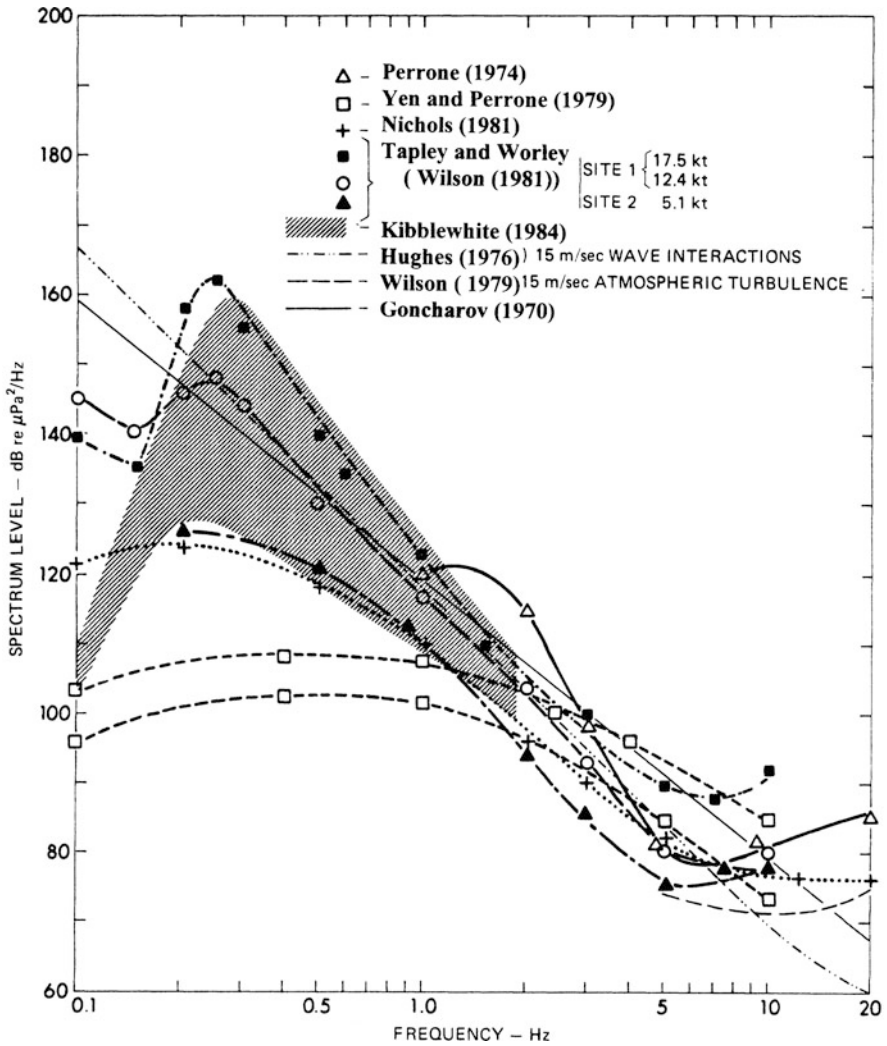
Fig. 4.3 Summary of infrasonic measurements and theoretical estimates [adapted from Kibblewhite and Ewans (1985)]

any doubt that wave–wave interactions produced the oceanic noise levels at frequencies between 0.1 and 5 Hz with an experimental spectral peak twice that of the surface wave height spectrum. The spectrum was observed to decrease steeply, probably a consequence of his experimental location. Nevertheless, the extrapolation to the open-ocean noise field was comparable to the estimates of Hughes, shown in Fig. 4.3.

The Sonic Region

Kerman (1984) showed that "the amalgamated observations of the ambient noise reveal a similarity structure, both in the acoustic spectrum and wind dependency." For frequencies greater than the local maximum in the 300–500-Hz region, Kerman found that the normalized measured spectral characteristic was proportional to f^{-2}
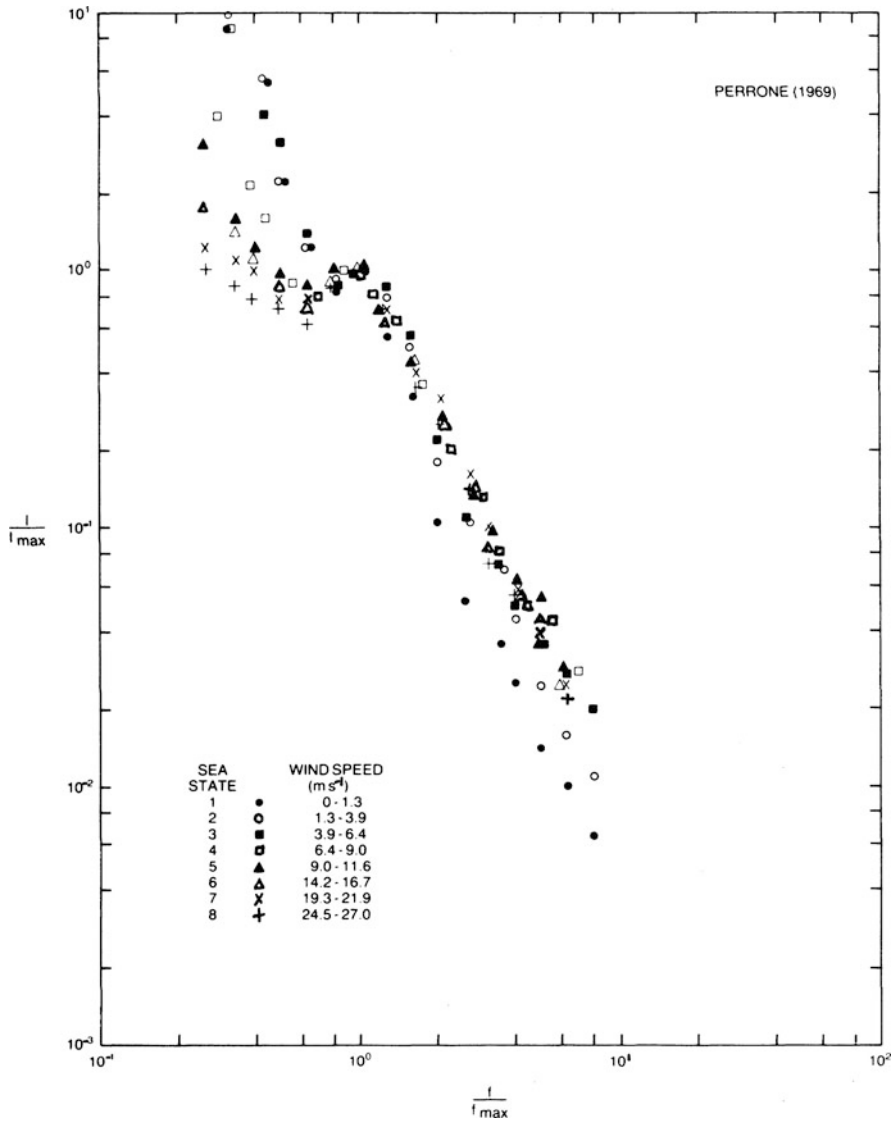

Fig. 4.4 Relative noise intensity versus relative frequency for the results of Perrone (1969) Kerman (1984) for a variety of wind speeds

(6 dB/octave), (Fig. 4.4). Furthermore, he showed that the noise intensity was proportional to the cube of the friction velocity (u_*^3) prior to a critical friction velocity (u_{*c}) determined by the minimum phase velocity of the gravity–capillary waves. Wave breaking was associated with this critical condition, and for $u^* > u_{*c}$, the noise intensity was found to increase with $u_*^{1.5}$ (Fig. 4.5) (see Chapter 2). The results shown in Figs. 4.4 and 4.5 represent a significant extension of Wenz curves for ambient noise levels.

Kerman concluded that the two distinct regions of ambient noise wind speed dependency existed, and suggested the presence of two sound source generation mechanisms or one mechanism that changed sensitivity. Since breaking waves were known to produce bubbles, spray, and splash, combinations of these mechanisms can explain the production of sound at frequencies greater than 500 Hz. Before wave breaking, bubbles can be produced by hydrodynamic surface instabilities and, consequently, one may have one mechanism that changes intensity since wave breaking produces more bubbles and consequently more sound. Kerman observed variability in the region below 500 Hz, consistent with Wenz.
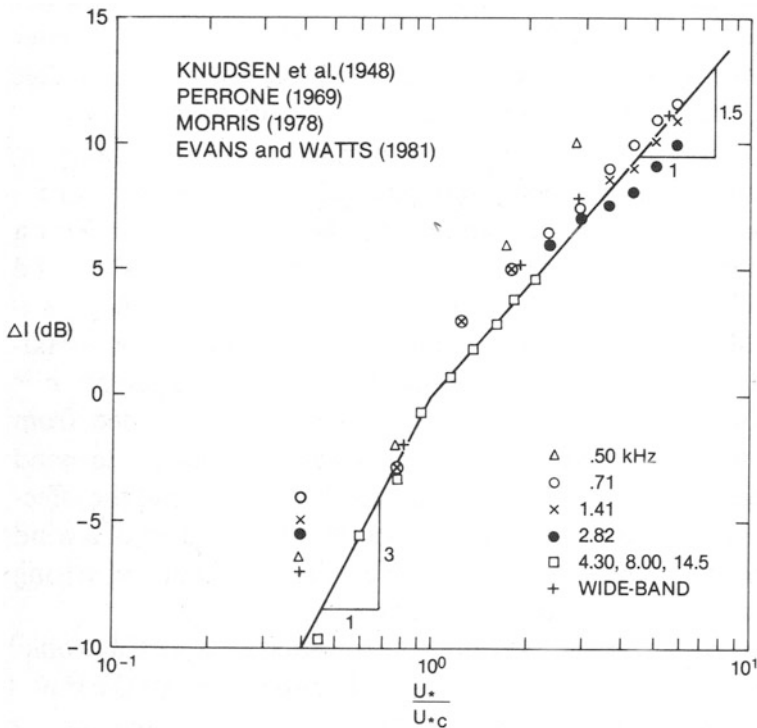

Fig. 4.5 The change in intensity level as a function of normalized friction velocity. Prior to the critical friction velocity there is one wind dependence, and for friction velocities greater than critical, there is another. The critical friction velocity is determinative of wave breaking Kerman (1984)

Before wave breaking, Kerman showed that the noise intensity was proportional to the cube of the friction velocity (u_*^3) prior to the critical friction velocity (u_{*c}), and for $u^* > u_{*c}$, the noise intensity was found to increase with $u_*^{1.5}$. The result is shown in Fig. 4.5 and the two wind speed regions are important to the estimation of ambient noise source level curves.

At frequencies less than 500 Hz, it was difficult to acquire ambient noise measurements attributable solely to local sources. The reasons for this difficulty were the dominance of noise radiated by shipping, the problems of measurement system self-noise, the size required for directional measurement, and the relatively low long range propagation loss. Figure 4.6 shows a comparison of measured noise spectrum levels ranging from 1 to 400 Hz, the very low frequency to high-frequency region. The observations presented in this summary are consistent with the observations of Wenz insofar as the region between 1 and 5 Hz shows a steep spectral slope (−5 to −10 dB/octave) with a wind speed dependence and a region above 100 Hz with a weak wind speed dependence, except for the measurements by Frisch in the Mediterranean Sea. The region between 5 and 100 Hz is basically wind-independent and the variation in levels is apparently determined by basin size and shipping density.

However, very low frequency to mid-frequency (1–500-Hz) ambient noise measurements that were not dominated by noise radiated from shipping at these frequencies showed the presence of locally wind-generated noise. Wittenborn (1976) found wind speed dependence with linear velocity dependence prior to u∼6 m/s and a nonlinear dependence at greater wind speeds. The results are shown in Fig. 4.7 for the frequency range of 1–500 Hz. The experiment consisted of a vertical string of omnidirectional hydrophones; one was positioned below the sound channel's
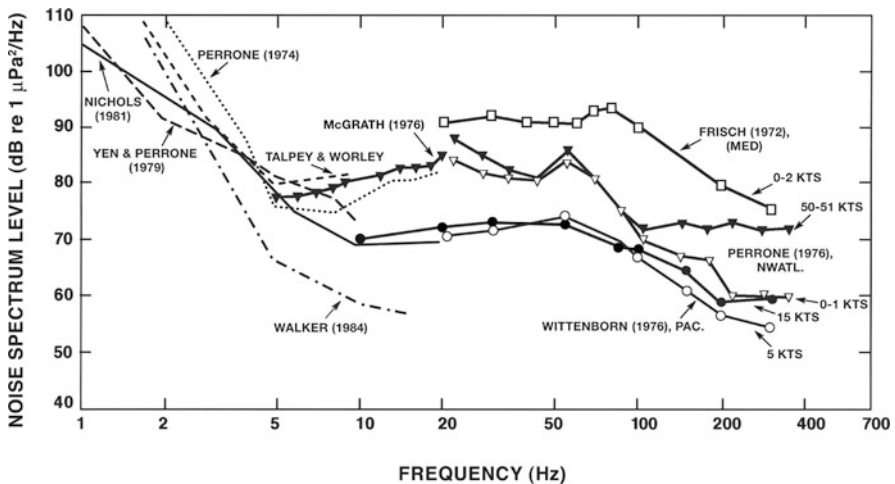

Fig. 4.6 Comparison of noise spectrum levels in the frequency range from 1 to 400 Hz in several ocean basins
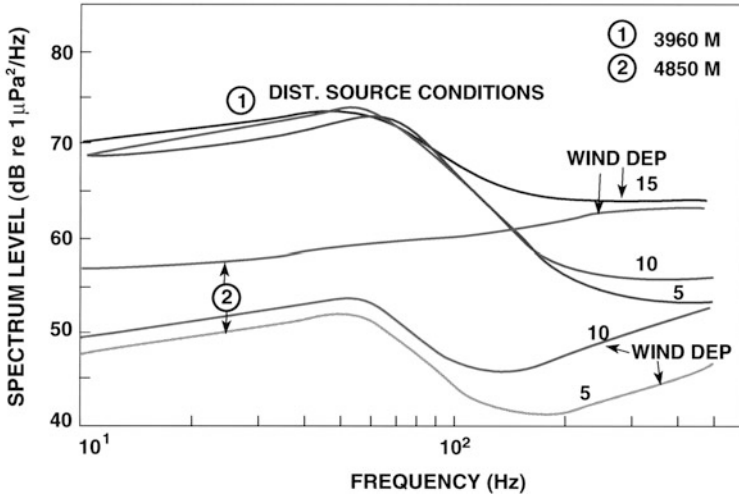
Fig. 4.7 The noise spectrum level from 1 to 500 Hz for a near-bottom hydrophone [adapted from Wittenborn (1976)]

critical depth to minimize the hydrophone's reception of distant generated noise, whereas the other was positioned in the sound channel. [Results were republished by Shooter, De Mary, and Wittenborn (1990).] The hydrophone data were recorded remotely on a time-indexed magnetic tape and wind speed estimates were based on interpolating weather reports of ships transiting the area. Stationary periods were selected by examining the continuous recording of the 300–500-Hz band of the deep hydrophone. The results clearly show wind-dependent noise characteristics between 1 and 500 Hz. The important feature, shown in Fig. 4.7, is that before wave breaking (wind speed about 10 knots), the ambient noise levels on the deepest hydrophone have a characteristic consistent with noise leakage from the sound channel.

After wave breaking occurs, the noise level measured by hydrophones below the critical depth for a wind speed of 15 knots is increased by 15 dB over the 1–500-Hz band. The hydrophone signal at the sound channel depth was still dominated by the noise from distant ships. This observation shows low-frequency sound is produced in breaking wave events. The low-frequency sound from breaking waves breaking is most likely due to microbubble plumes and clouds associated with breaking waves.

Observations in the sparsely shipped Southern Hemisphere represent measurements not dominated by shipping. Kibblewhite (1976) compared the levels between the North Pacific and the South Pacific as shown in Fig. 4.8. The relative difference in levels is striking between 15 and 200 Hz. Cato (1976) examined 40 sites near Australia and found wind speed dependence between 20 and 5,000 Hz. His measurements also included the effects of moderate shipping and considerable biological activity.

Measurements performed with vertical arrays in the sparsely shipped Southern Hemisphere's Fiji Basin [Bannister (1981), Burgess and Kewley (1983), Browning
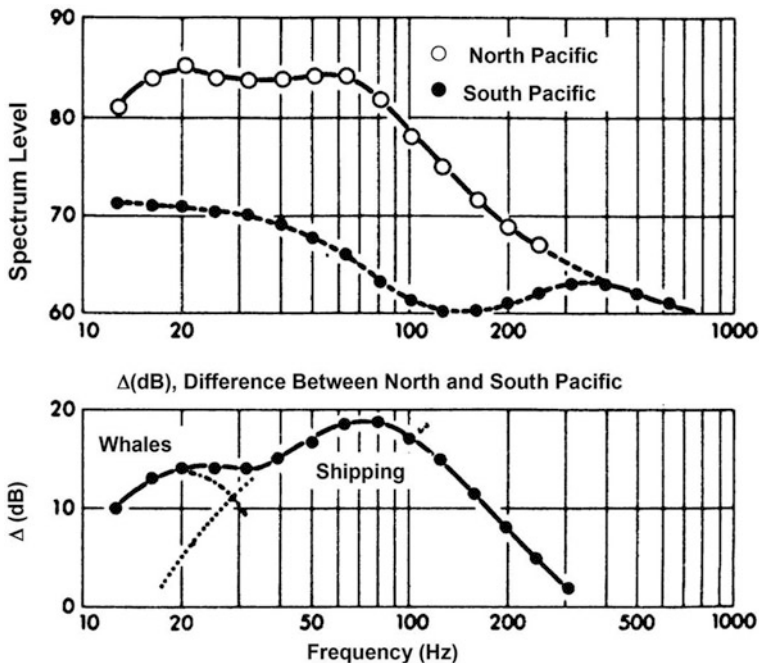
Fig. 4.8 Comparison of measured noise levels in the North Pacific and the South Pacific. [Kibblewhite (1976), note the ordinate label should be "Spectrum level $dB\,re\,(\mu Pa)^2/Hz$."]

(1986)] were also found to have low-frequency wind noise with two distinct wind speed dependencies. When compared with other shallow water and deepwater noise measurements, these results led to the conclusion that at lower frequencies sound was generated near the sea surface with one wind-speed-dependent mechanism prior to wave breaking and another after wave breaking. Since field observations are dependent on the mechanism of sound production at the sea surface and sound transmission is determined by environmental factors such as water depth, bottom properties, and the sound velocity structure, the measured noise levels can be variable. The conclusion, however, was that in the low- to high-frequency region, the noise characteristics were determined not only by propagation but also by whether shipping or breaking wave sources of sound are dominant. The question posed was: How does a breaking wave produce low-frequency sound?

Two interesting experiments have been performed featuring visual as well as acoustic identification of wave breaking events. Hollett (1988) performed an experiment in the Mediterranean Sea with a vertical array of hydrophones (three nested apertures (32 phones each) with center frequencies at 375, 750, and 1,500 Hz) and simultaneous video recording of the sea surface area intersected by the end-fire beam of the array. Figure 4.9 shows the spectral events resulting from a large spilling breaker. The spectra shown have not been corrected for the prewhitening of
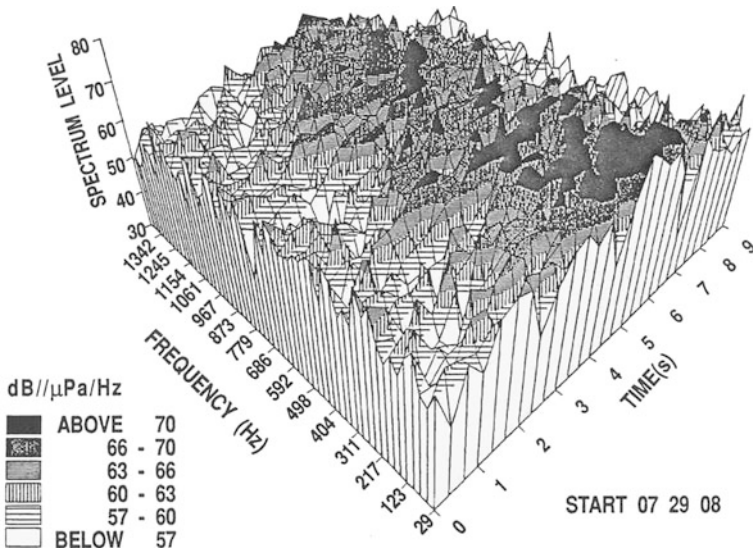
Fig. 4.9 Spectra of a wave breaking as measured by Hollett (1992) as a function of time. The lower-frequency spectral estimates have not been corrected for pre-emphasis. This collection of acoustic spectra shows the wave-breaking event to be a random collection of spectral peaks

the data; i.e., the lower-frequency spectral content is more pronounced than shown. The breaking event occurs between 3 and 7 s and is seen to be a random collection of spectral peaks most pronounced in the low-frequency (below 300 Hz) range.

Thus, a plausible explanation is that at higher frequencies single bubble noise is important. At lower frequencies, the collective oscillations of regions with sufficient compressibility are responsible for the sound. These radiations are described by the oscillations of these regions as if they were single radiators and have frequencies described by a modified Minnaert equation (see Chapter 3 or Appendix D). Farmer (1989) performed an experiment in 200 m of water with a hydrophone 14 m below the surface and was able to identify the occurrence of wave breaking by examining the video obtained from a subsurface camera. The simultaneously recorded acoustic data were examined and found to show that the breaking waves radiate sound to frequencies as low as 50 Hz.

The Hollett and Farmer results show that breaking waves are a source of low-frequency sound and that at frequencies below 500 Hz the ambient noise spectrum in the absence of shipping is wind-speed-dependent. These results are important with respect to measurements performed with vertical and horizontal arrays, where the directional noise properties, in the absence of shipping, are due to the interaction of wind-generated noise and the basin boundaries.

The Wind Speed Dependency at Frequencies Less Than 500 Hz

The wind speed characterization was based on the determination of two parameters, the spectral slope m(f) and the wind speed dependency n(f) defined by

$$\Delta NL(f, f_o U, U_o) = 20n(f)\text{LOG}(U/U_o) + 10m(f) \cdot \text{LOG}(f/f_o), \qquad (33)$$

where ΔNL is the difference in measured noise level at frequencies f and f_o for wind speeds U and U_o. These parameters are estimated by the use of regression analysis and, in some instances, by visual least-squares estimation. As stated previously, the measurement of low-frequency wind-dependent noise is difficult owing to the presence of shipping noise, self-noise, and sound propagation conditions.

Shown in Fig. 4.10 is the problem of determining n(f) in the case of a two-component noise field, shipping- and wind-dependent surface noise. When the curve is horizontal, n = 0, no wind speed dependency, shipping noise dominates. At low frequency, n(13 Hz) = 2.10, for higher wind speeds n(283 Hz) = 1.36, and then n decreases to n(2.2 kHz) = 1.20.

The frequency-dependent characteristic of n(f) was observed in other experiments (Fig. 4.11). n(f ≤ 40 Hz) ≈ 2.6, but n(f ≥ 300 Hz) ≈ 1.2.
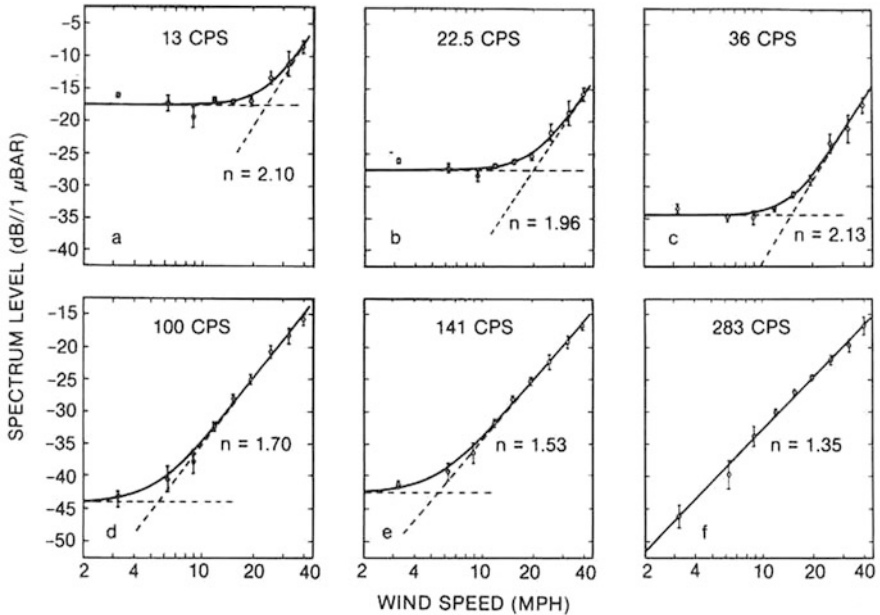

Fig. 4.10 Frequency-dependent wind speed characteristic for several frequencies. The *horizontal lines*, no wind speed dependence, at lower frequencies and low wind speed show the limiting effect of noise from distant shipping. [(Piggott 1964), note the ordinate label should be "Spectrum level *dB re* $(\mu Pa)^2/Hz$" and is obtained by adding 100 dB.]
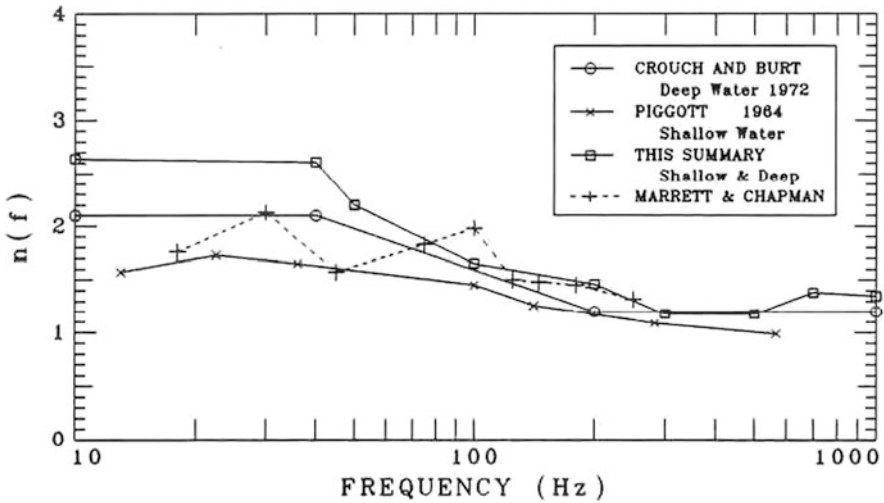
Fig. 4.11 Wind speed dependency factor n(f) versus frequency for wind speeds above 13 knots. Shown are the results of Crouch and Burt (1972), Piggott (1964), and Marrett and Chapman (1990), and an average of all results

In the previously discussed Wittenborn (1976) experiment, a vertical string of omnidirectional hydrophones found a wind speed dependence with a linear velocity dependence prior to u∼6 m/s and a nonlinear dependence at greater wind speeds. The 15-knot curve from this experiment, Shooter et al. (1990), in Fig. 4.12 has spectral slopes of m = 0, m = 1, and m = 1/3. The corresponding wind speed factor (n), determined by the difference in noise levels at 12 and 15 knots for a frequency of 100 Hz, was n = 1.65.

Several investigators have used vertical arrays to measure the locally generated noise in deep water. Most notable are the works of Burgess and Kewley (1983) in the South Fiji Basin and Australian waters, and Kennedy (1990) in the Tongue of the Ocean near the Bahamas. In addition to the use of steerable arrays, these experiments were conducted in areas to minimize shipping noise and had concurrent measurement of wind speed. The Burgess and Kewley (1983) experiment used a 180-m steerable array at a depth of 300 m in deep water to avoid mixed-layer ducting effects. Upward- and downward-looking beams were used to estimate the source level (dB *re* 1 $\mu Pa^2/(sr \cdot Hz)$) at the sea surface. Since their original publication, these authors have reexamined their linear regression analysis of the wind speed dependency and have concluded that two wind-speed-dependent regions exist, i.e., one prior to and one after the onset of wave breaking with n∼1.5 (Kewley et al. 1990).

The frequency-dependent source level estimate is shown in Fig. 4.12. In examining Fig. 4.12, one must differentiate between noise level and source level estimates that have been plotted on the same scale to show that there is no strong spectral dependence at wind speeds greater than 6 m/s (12 knots). In the case of the Kewley (1990) results, we observe at most m = 1/3 between 100 and 200 Hz.
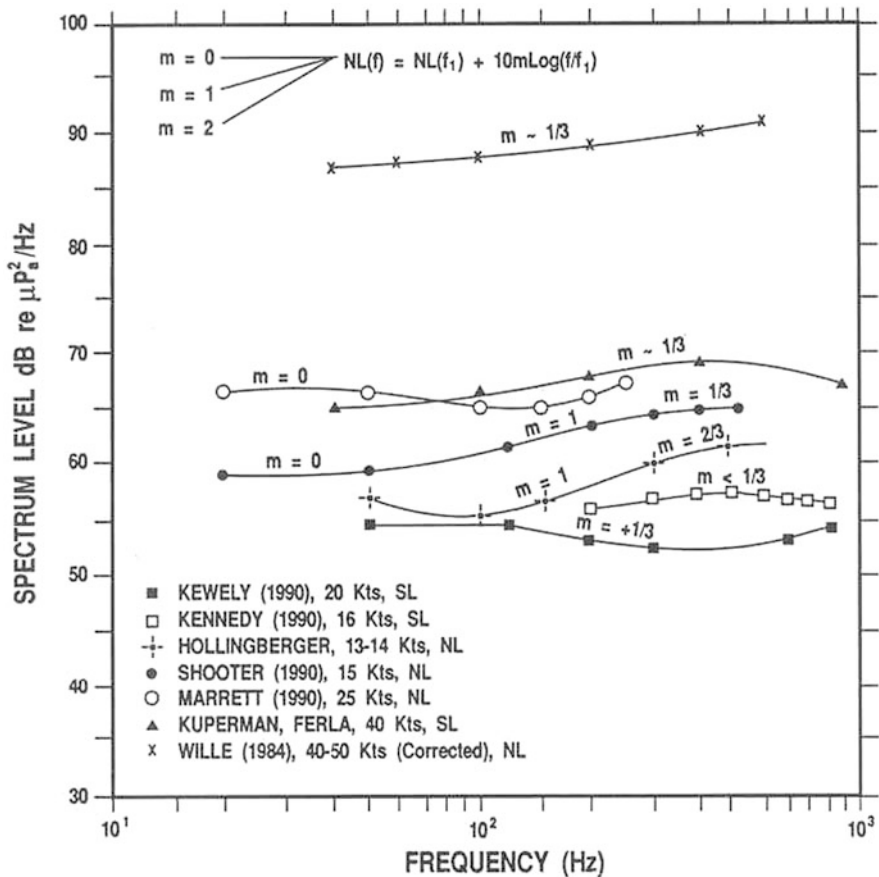
Fig. 4.12 Source spectrum level (SL) and noise spectrum level (NL) versus frequency for wind speeds above 13 knots for several diverse oceanographic areas

The Kennedy (1990) experiment was performed with a measurement array of seven-octave nested four-wavelength linear apertures covering the 40–4,000-Hz band. Meteorological measurements were performed on the nearby Andros Island. The measurements were made at a considerable height above the land surface of the island and were used to estimate the critical speed at the ocean surface at the measurement location. In his experiment, Kennedy was able to model the propagation in the Tongue of the Ocean. The vertical distribution of ambient noise $N(\theta)$ can be written as (Talham 1964)

$$N(\theta) = dI/d\Omega = DPWg(\theta\,') \exp(-2\alpha r)/\cos\theta\,'(1 - \beta\gamma \exp(-4\alpha r)), \qquad (34)$$

where $W = [\sin\theta'/\sin\theta] = [C_s/C_r]^2$, D is the source density at the surface (number/m^2), P is the power (W/sr), $dI/d\Omega$ is the intensity per unit solid angle
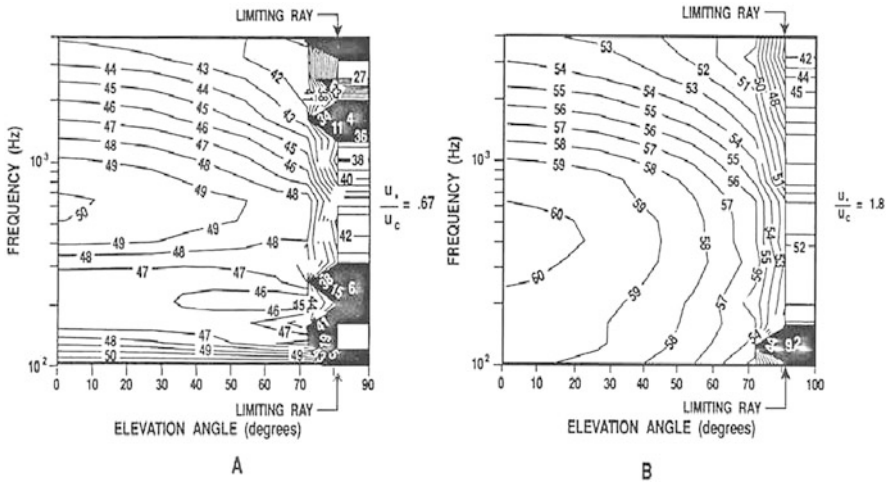
Fig. 4.13 Estimated noise spectrum level versus elevation angle as estimated by Kennedy (1990) for **a** before wave breaking and **b** after wave breaking

(W/m²/sr), α is the frequency-dependent absorption coefficient, γ is the surface reflection coefficient, β is the reflection coefficient of the bottom, θ' is the source angle, θ is the angle at the receiver, and C_s and C_r are the speed of sound at the source and the receiver, respectively.

Thus, given knowledge of the environmental factors, one could estimate $g(\theta')$ given a measurement of $N(\theta)$. Kennedy measured $N(f, \theta)$ and determined, with a similar but more complicated method of curve fitting, the best fit to $D \cdot P \cdot g(\theta')$. Kennedy's results (Fig. 4.12) for a wind speed of 8 m/s (16 knots) show a practically white spectral curve. The novel aspect of Kennedy's experiment was his ability to estimate the source directional characteristic $g(\theta')$ as a function of wind speed and frequency. Shown in Fig. 4.13 are two examples of $N(f, \theta)$ from this estimation based on his measured data. Figure 4.13a shows the estimated pattern at low wind speeds prior to whitecaps being present. A broad local maximum is observed at 600 Hz that decreases with an increase of elevation angle ($0°$ downward), vertical directionality. At lower frequencies, the level is rather constant with elevation angle; no directionality was observed. Kennedy found with whitecaps present (Fig. 4.13b) a broad downward-directed maximum at 400 Hz consistent with the vertical directionality from a surface distribution of dipole or doublet sources over the entire frequency range.

The structure shown in Fig. 4.13a was modeled by dipoles near the broad maximum at 600 Hz, but at lower frequencies (below 300 Hz) the structure was consistent with distributed sources or noise from a distance. The structure presented in Fig. 4.13b was found to be consistent with dipole or doublet distributed sources, monopoles beneath the pressure-release surface. Kennedy's results show a slowly varying spectrum level with frequency, but also vertical directionality consistent

with a dipole or doublet radiation characteristic of sound generated near the sea surface associated with wave breaking.

Marrett and Chapman (1989) performed measurements of low-frequency (15–250-Hz) ambient noise in the South Fiji Basin with a towed line array. Local wind speed measurements were performed. Shown in Fig. 4.12 are the 25-knot noise level results. The spectrum again has a fairly white character. For wind speeds greater than 15 knots, the wind speed dependency factor was found to be n≃1.32 at 250 Hz and n≃2.13 at 30 Hz.

These deepwater ambient noise measurements show that for wind speeds greater than 6 m/s, the sea surface sound has a slowly varying spectral shape with a broad maximum ranging from 300 to 500 Hz. The results from three additional shallow water experiments are shown in Fig. 4.12. Ferla and Kuperman (1984) reported results on the wind-generated source spectrum levels for wind speeds between 10 and 40 knots. They used propagation loss measurements and environmental information in a wave-theoretic noise model to derive these source levels from measured noise levels. As can be seen, their results are consistent with the deepwater curves. Also shown are results from Wille and Geyer (1984) in the North Sea at 40–50 knots and Hollinberger and Bruder (1990) in an Alaskan fjord at 13–14 knots. To obtain the curve attributed to Wille, an estimated but relative correction factor, based on measured propagation loss, was applied to the measured noise levels. All these results have similar spectral slope with frequency but different spectrum levels.

This characteristic of a broad maximum between 300 and 500 Hz has been recognized in wind-generated ambient noise for quite some time (Wenz 1962), (Piggott 1964), but was not identified with such a diverse set of experiments. The broad maximum between 300 and 500 Hz characteristic of the curves shown in Fig. 4.12 has a decreasing spectrum level as frequency decreases. This decrease corresponds to a spectral slope factor of m~1/3 or 1 dB/octave. This characteristic has often been compared to the relative spectrum of noise due to a spray of water droplets developed by Franz (1959). However, the Franz spectrum has a steeper (1.3–1.4 dB/active octave) slope than the spectra here; nevertheless, the observation of their similarity is worthy of detailed consideration.

Mid- to High-Frequency Wind Speed Dependence

In the previous discussion of low-frequency noise measurements, the wind speed dependency characterized by the factor n(f) was observed to range from 1.3 to 2.5. Wind speed has traditionally been used to provide an index for the level of noise to be expected at higher frequencies. But even at high frequencies, the wind speed dependency factor may be variable and complex. To illustrate the complexity of the wind speed dependency factor n, we have produced the schematic shown in Fig. 4.14. The data shown were obtained in the North Sea, a region with appreciable shipping-generated noise. The specific data set illustrates what was found in the literature concerning the wind speed dependency. The spectral curve at 20 kHz below
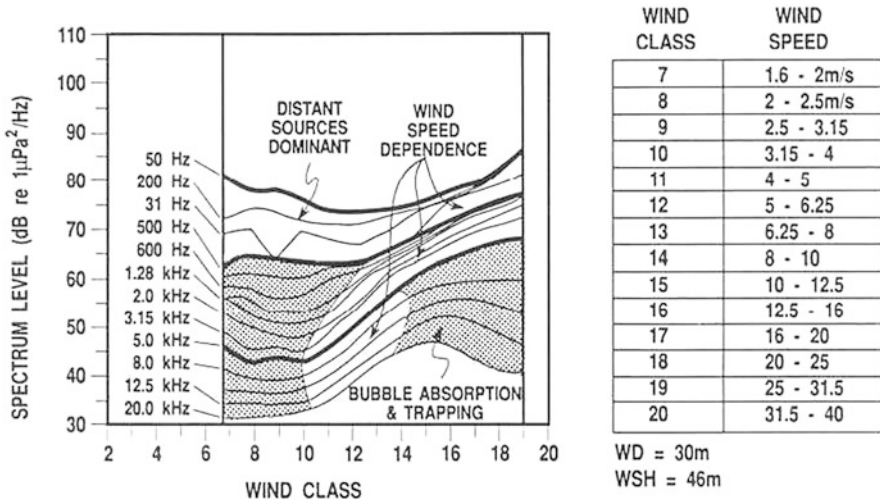
WIND CLASS	WIND SPEED
7	1.6 - 2m/s
8	2 - 2.5m/s
9	2.5 - 3.15
10	3.15 - 4
11	4 - 5
12	5 - 6.25
13	6.25 - 8
14	8 - 10
15	10 - 12.5
16	12.5 - 16
17	16 - 20
18	20 - 25
19	25 - 31.5
20	31.5 - 40

WD = 30m
WSH = 46m

Fig. 4.14 Spectrum level of ambient noise versus wind speed class in the North Sea. These spectra show the general wind speed dependency of ambient noise. [Adapted from Wille and Geyer (1984)]

a wind speed class of 10 shows no dependency (n = 0); between wind speed classes 11 and 13, there is a dependency of n = 2; and at higher wind speeds, there is a reversal of slope and a decrease in noise level.

This trend is seen to persist in some degree down to 5 kHz. The decrease in sound level at wind speeds greater than 10 m/s has been attributed to sound absorption by the near-surface microbubble layer and trapping in the near-surface sound duct produced by sound speed gradients resulting from the presence of microbubbles (Wille and Geyer 1984), Farmer and Vagle 1989).

At 1 kHz, we observe a region of no wind speed dependence below a wind speed class of 12 and a wind speed dependency of n = 1.75 at greater wind speeds. At lower frequencies, about 200 Hz, a wind speed dependency is only observed for higher wind classes (wind class above 16, wind speed above 12.5 m/s). In general, the observed wind speed dependence was a noise-limited region, a transition region, and a high-wind-speed region. These regions are shown in Fig. 4.15 for representative wind speeds and values of *n*. Classifying measurements in these regions may aid in the interpretation of low-frequency noise levels and may explain the variation found in the published values of *n(f)*.

This scheme has been used to examine the value for *n(f)* for noise results obtained at wind speeds greater than 6.5 m/s for selected experimental results. The summary of this analysis is shown in Fig. 4.11 along with the values reported by Crouch and Burt (1972), Piggott (1964), and Marrett and Chapman (1990). The trend is clear for high winds speeds; n(f) has a constant value of about 2.5 until a frequency of 50 Hz and about 1.2 for frequencies greater than 300 Hz. The variation of n(f) with frequency between 50 and 200 Hz appears to be real. Kerman (1984) observed that all high-frequency results (above 500 Hz) yield a consistent set of characteristics.
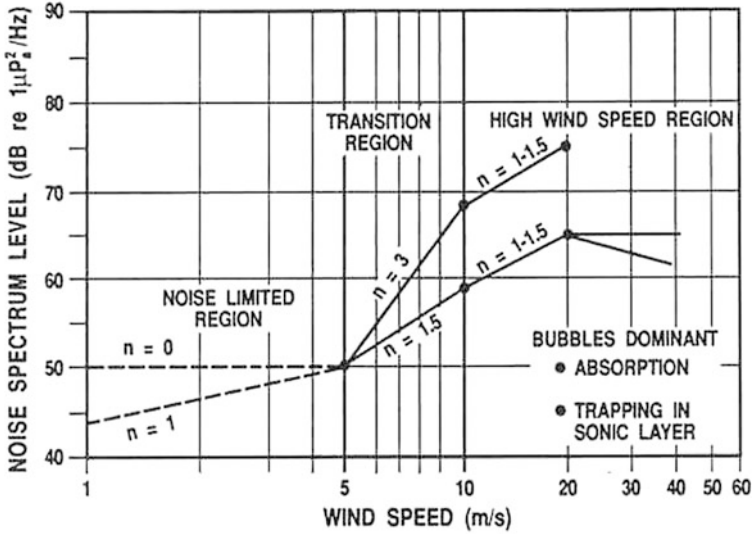
Fig. 4.15 Wind speed dependency ($n(f)$) versus wind speed for frequencies below 20 kHz. Three regions are identified: a noise-limited region, a transition region, and a high-wind-speed region

This indicates that sound production at these higher frequencies may be from the same mechanisms, such as bubble, splash, and spray. However, the variation of $n(f)$ at lower frequencies indicates a different mechanism before and after wave breaking.

Low-Frequency Noise Characteristics

One now has an answer to the question "What are the characteristics of low-frequency (below 500 Hz) ambient noise?" First, the cited evidence showed breaking waves produce sound with frequency as low as 30 Hz. The Hollett spectra appear to be a random collection of spectral peaks spread in frequency and time during the breaking event. These results are similar to those of Farmer (1989), although in some instances Farmer observed a broadband event representative of impact noise at the beginning of the wave breaking, followed by the subsequent random collection of spectral peaks.

Second, we showed that measurements of local wind-generated noise at wind speeds greater than 6 m/s have a broad maximum between 300 and 500 Hz. The position of this maximum shifts to lower frequencies as the wind speed increases. The decrease in spectrum level with a decrease in frequency is less than m = 1/3 (1 dB/octave) below this broad maximum.

Third, we showed that the wind speed dependency ($n(f)$) of local wind-generated noise is a complex function and may be characterized by three regions. In the high-wind-speed case, the low-frequency noise level (dB *re* 1 μPa^2/Hz) increased with wind speed dependency $n(f) = 1.5$ at 200 Hz, which ranged between 1.3 at 500 Hz and 2.5 at 30 Hz.

Finally, the results of Kennedy (1990) clearly show that low-frequency sound produced at the sea surface after the occurrence of wave breaking has a dipole radiation characteristic. Thus, the problem is reduced to finding a sound-generating mechanism that produces a broadband event followed by a random collection of spectral events, which scale according to $U^{2n(f)}$ power.

Directionality

The directionality of the oceanic noise depends on the source of the sound and the frequency-dependent propagation factors. Sources of sound near the surface of the sea have a dipole characteristic as discussed in Chapter 1 and Appendix G. Bubbles and bubble clouds are subsurface monopoles, and because of the surface image effect as well as the near-surface bubble-layer attenuation are always essentially "dipolelike." That is to say, at lower frequencies, oscillating bubble clouds caught in the orbital motion of the gravity wave field have a dipole characteristic. In the frequency region where single bubbles dominate the noise, one has a dipole characteristic at low wind speeds due to the image effect, whereas at higher wind speeds the combination of the image effect and the exponentially distributed bubble layer produces radiation patterns in the downward direction that can be considered "dipolelike." Furthermore, spray and splash of breaking waves act as dipole sources of sound.

Propagation of sound in the ocean determines the range at which noise sources are important. In both deep and shallow water, noise radiated at the surface in the high-frequency range is attenuated by the absorption in the seawater and boundary interactions, the rough sea surface and bottom. At lower frequencies, the attenuation decreases, the range of influence becomes larger, and reflection loss from the bathymetry is less. For example, propagation of sound near 50 Hz ensures that the reflection from slopes and seamounts is important because of the high bottom reflectivity. Owing to the angle of the slope, the downward-directed energy from the source of sound will reflect from the boundary with a reduction in angle of twice the slope angle. This reduction of the angle of propagation couples sound over bathymetric features into the sound channel. The consequence is a slope enhancement, the megaphone effect, and is profound for both surface-ship- and wind-driven noise at lower frequencies.

Low-Frequency Directional Noise Characteristics

Omnidirectional measurements of mean square pressure and its logarithmic counterpart, the ambient noise level, as stated previously, were usually made with a filter, a squaring device, an integrator, and an incoherent sum or averaged. Recent measurements were performed by digitizing the noise signal and taking the linear average of the FFT magnitude squared and then sequentially averaging the results. Both methods yield sample measures of the mean square pressure, the mean

intensity, and variance that can be converted to an ambient noise level. The omnidirectional hydrophone spatially integrates the multiple sources of noise, the number of which, in any given time period, can be large and variable. The mean ambient noise levels can vary by as much as ± 6 dB depending on the processing and averaging actually employed; however, the mean ambient noise levels are predictable from location to location with wind speed and shipping densities as controlling parameters.

Array processing can be accomplished either in the time domain or in the frequency domain. In the time domain, the hydrophone signals are amplified, summed after a suitable steering time delay has been applied, and then filtered, squared, and averaged as before. Shading may be applied to control side lobes. In the frequency domain, the signals are Fourier-transformed in the temporal and spatial domains to yield an equivalent beam power. Thus, one might expect levels analogous to the omnidirectional levels because the broad beams still contain many sources and multiple paths.

On the other hand, high-resolution arrays that resolve individual noise sources have dramatically different spatial and temporal characteristics. In the omnidirectional case, the mean square pressure is the squared sum of a large number of random components, whereas in the resolved case, the observable is the squared superposition of individual coherent components and a lower-level random component. The measurement of the directional characteristics of the noise field is a development since the work of Wenz.

Beam Noise Levels and Horizontal Directionality

The measurement of horizontal noise directionality (beam noise level versus angle) is at best difficult since measurements performed with horizontal line arrays have a left–right ambiguity. Because of this ambiguity, the measurement of the horizontal directionality requires either a deconvolution technique on the array beam-former output or the use of bathymetric shielding.

Wagstaff (1978, 1981, 2005) developed such a technique and used it to characterize the noise directionality in several ocean basins, such as the Northwest Atlantic, the Northeast Pacific, the Indian Ocean, and the Mediterranean Sea. The technique was approximate and required a directional array towed in a hexagonal pattern. The method involved iterative convolutions between an estimated field and the measured patterns until a least-squares criterion was achieved. The technique required approximately 20 h to perform and, thus, the estimated directionality was termed the "persistent component" of the low-frequency noise field. The hypothesis of Wagstaff was that the shipping densities, propagation of sound, and the bathymetry determine the directionality, and that this was a characteristic of each basin. In particular, he was mindful of the "megaphone effect" (6 dB) and concluded that surface ships over the continental slope were very important since shipping lanes usually proceed from the deep ocean to ports in a predictable pattern. This did not imply that fishing, continental shelf activity, the presence of oil wells, and exploration activity were ignored.

This approximate deconvolution method was evaluated in several sea tests during which the shipping density as a function of latitude and longitude was determined by over flights, the range-dependent sound propagation was measured, and the meteorological conditions and oceanic variables were known.

For frequency bands centered on 50 and 150 Hz, Fig. 4.16a shows results from a location near the Corner Seamounts in the Northwest Atlantic Basin, whereas Fig. 4.16b shows the results for the Gulf of Mexico for an array towed off the Yucatan Peninsula. For the Northwest Atlantic Basin, observe the 7.6–15-dB anisotropy, with the highest levels in the north–northeast, north and northwest; that is, in the direction of the major shipping lane (north, north-northwest), the Scotian Shelf and Halifax Harbor (north-northwest), and Grand Banks (north-northeast).
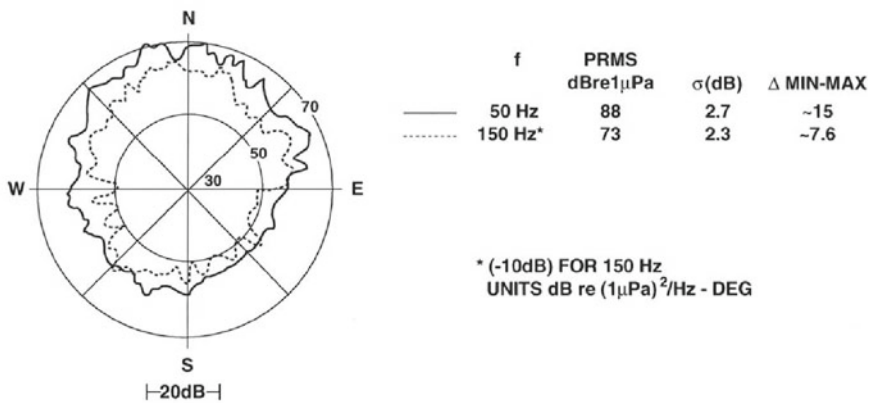
a.) The Northwest Atlantic
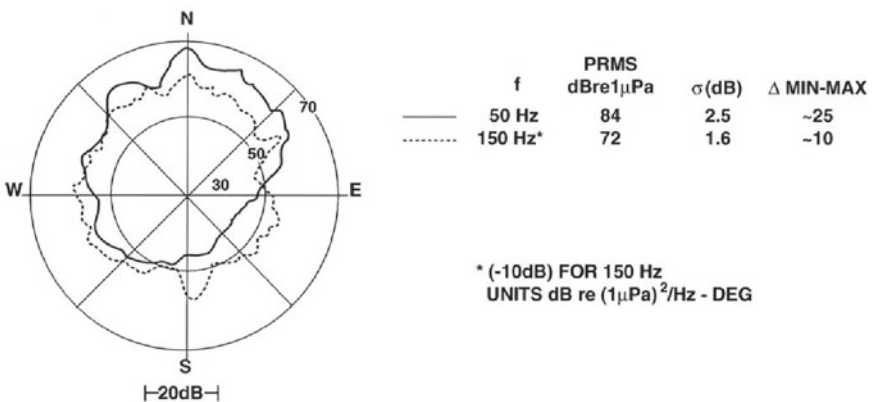
b.) The Gulf of Mexico

Fig. 4.16 Horizontal noise directionality: (**a**) the North Atlantic and (**b**) the Gulf of Mexico

The observed directionality was attributed to shipping, both mid-basin and traversing the continental rise shelf and Grand Banks. Also shown in this figure are the omnidirectional noise levels as well as the standard deviation derived from measured and estimated beam levels used in the estimation procedure.

The estimate of the horizontal directionality for the Gulf of Mexico showed high levels in the northern quadrant and low levels in the southern quadrant in the direction of Campeche Bank. Again, the difference between high and low levels was found to be 10 dB at 150 Hz and 25 db at 50 Hz, with pooled standard deviations of 1.6 and 2.5 dB, respectively. The northern quadrant contains the ports of Galveston and New Orleans, and oil-platform activity. Wagstaff showed that this long-time averaged pattern, the persistence, was correctly described by calculations provided that the shipping densities were known, transmission was calculable, and that ships over the continental shelves and seamounts were included. He showed that the megaphone effect coupled with shipping dominated these horizontal directional patterns.

Beam noise level time series were also obtained with an array using a plane wave beam-former and continuously recorded hydrophone signals in the Levantine Sea (4 h) and the Ionian Sea (10 h).

Figure 4.17 shows an example of the Levantine Sea beam noise levels versus the azimuth angle and time for a frequency of 320 Hz, a 110-wavelength aperture, a bandwidth of 0.18 Hz, and a sample time of 8 s, with the grayscale span of 40 dB normalized to the peak level. The shipping traffic, which is the marked by darker lines, is well tracked. This aperture resolves the shipping and provides a contrast
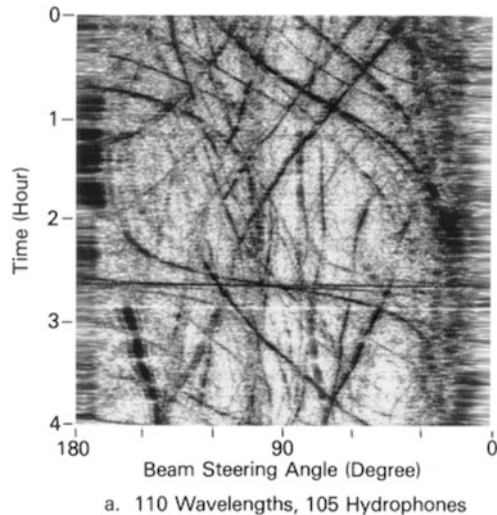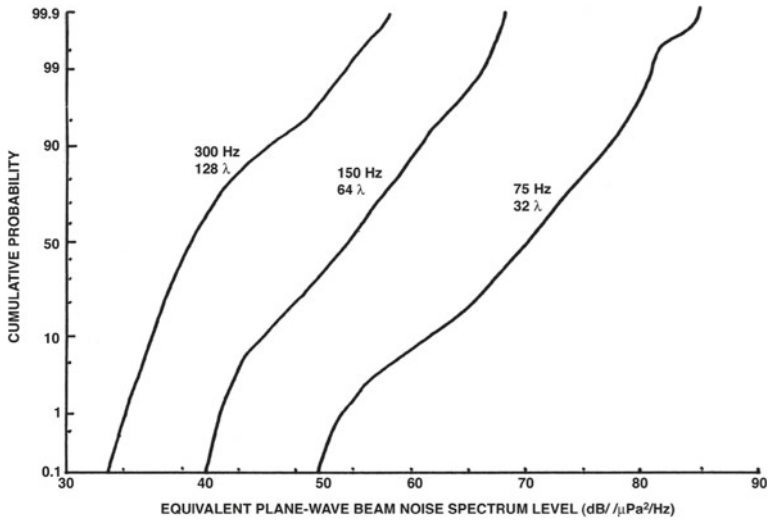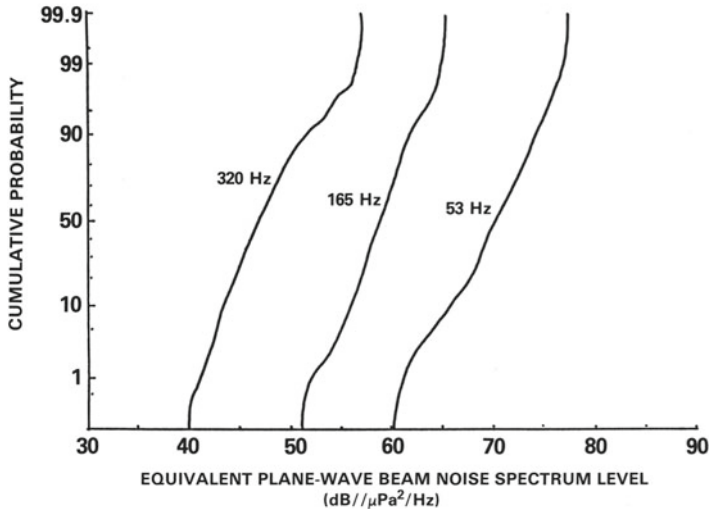

a. 110 Wavelengths, 105 Hydrophones

Fig. 4.17 Beam noise intensity levels versus time and steering angle for a frequency of 320 Hz, 0.18-Hz bandwidth, and 8-s interval

A. The Ionian Sea Cumulative Distribution Function

B. The Levantine Sea Cumulative Distribution Function

Fig. 4.18 Cumulative distribution functions for array beam noise levels for the Ionian Sea and the Levantine Sea. Each beam output was normalized to the plane wave response of the system. Each beam noise level was determined from a 0.18-Hz bandwidth, an 8-s coherent integration time, and an incoherent average over 6 min

with the background noise, the lighter areas. The dynamics of the two-component noise field, shipping and environmental, are obvious.

Cumulative distribution functions were computed for various measurement parameters to quantify the statistical characteristics of beam noise. The cumulative distribution functions for three frequency bands with an integration time of 8 s showed insignificant differences. The beam noise autocorrelation function, using the complex FFT beam output, was used to determine the average decorrelation time, taken as the zero crossing, of 10 min. Cumulative distribution functions for the broadside to aft end-fire beams based on 6-min averages from the Levantine Sea and the Ionian Sea were found to have substantial differences. The Levantine site was close to major shipping lanes, whereas the Ionian site had a more uniform distribution of ships. These cumulative distribution functions are decidedly not log normal, and are consistent with the dynamical distribution of ships and the relative response of the beams and side lobes to their radiated noise.

Vertical Noise Directionality

In a deep cylindrical ocean basin, the sound velocity maximum near the surface decreases as the depth increases to a minimum, and then increases as the depth increases owing to the increase in pressure. This sound speed variation produces a sound channel between the surface maximum and the critical depth at which the speed of sound has reached the surface value. Figure 4.19 shows this variation for a representative basin with a continental slope (3–6°) and shelf.

Vertical array measurements such as those by Fox (1964) and Axelrod et al. (1965) showed at higher frequencies the deepwater noise directionality was primarily from surface-generated noise whereas at lower frequencies noise along the horizontal was observed Fig. 4.20. Cron et al. (1962, 1964) explained these measurements with space-time correlation functions derived from volume sources (isotropic noise) and surface sources (anisotropic noise) and showed the vertical directionality at higher frequency to be proportional to $\cos(\theta)^m$, where θ is the depression angle and $m = 1, 2, \ldots$. This type of analysis was extended by Cox (1973) with the utilization of spherical harmonics to derive the general space-time correlation functions that facilitated the estimation of pairwise covariance properties. His results agreed favorability with a variety of measurements and provided a method of determining the optimum spacing of array hydrophones.

Sound radiated from the surface or near the surface was consistent with dipole-like directional characteristics and produced a characteristic directional pattern on a vertical array. Talham (1964) derived an expression for the vertical directionality from surface noise sources incorporating the effects of absorption, refraction, and reflection as a function of receiver depth. This type of analysis shows downward, higher-angle, directed energy is absorbed by multiple interactions with the boundaries and results for a flat ocean basin in the arrivals being peaked at the SOFAR channel limiting angles (10–15° off the horizontal). However, as shown in
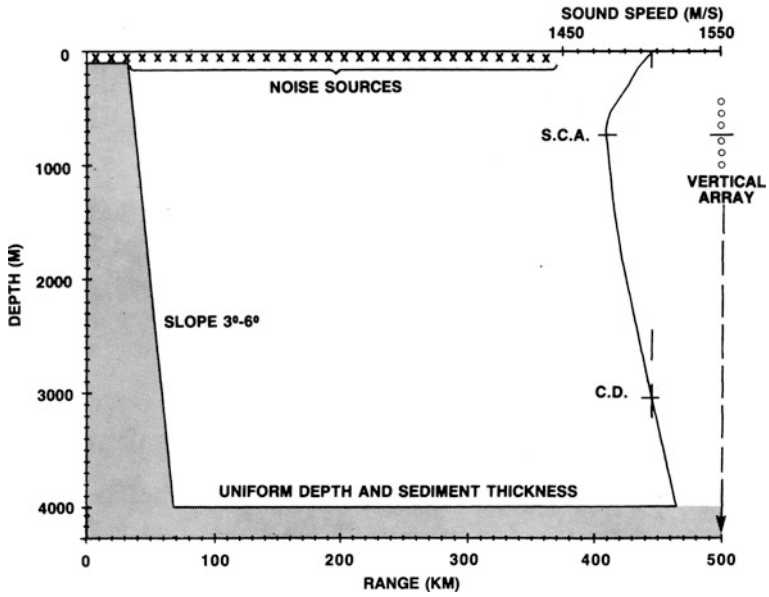
Fig. 4.19 The typical basin cross section with a deep water sound speed profile showing the sound channel axis and the critical depth
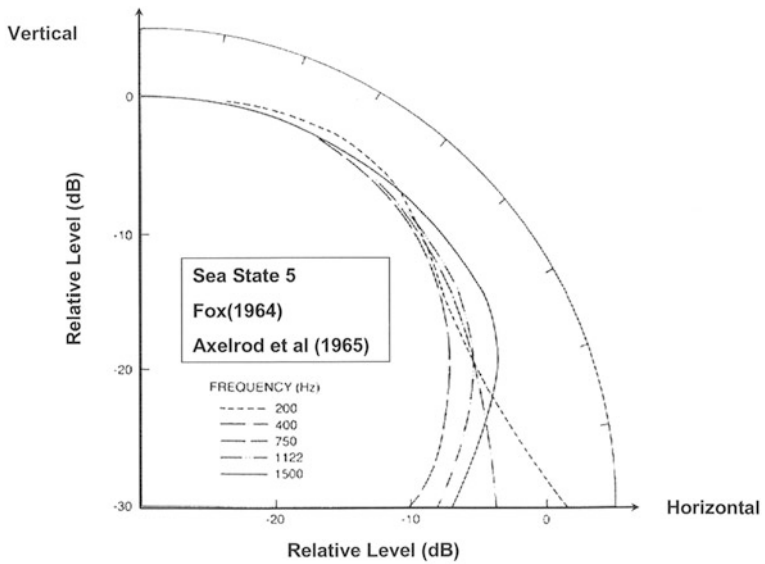

Fig. 4.20 The vertical directionality of noise, relative level (dB), versus elevation angle for frequencies between 200 and 1,000 Hz
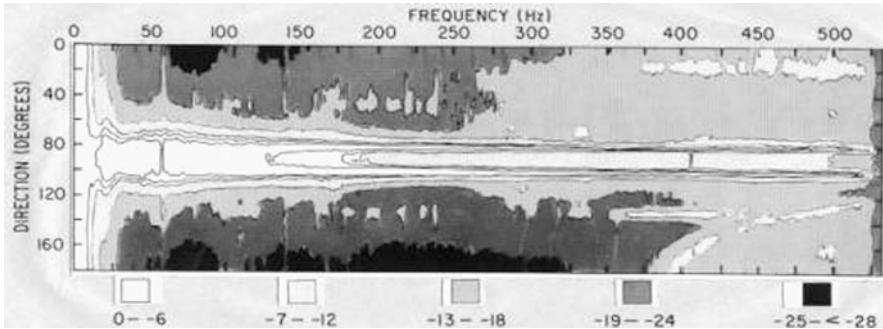
Fig. 4.21 The vertical arrival structure observed on an array in the sound channel as a function of vertical angle and frequency (Carey and Wagstaff (1986, Fig. 4)
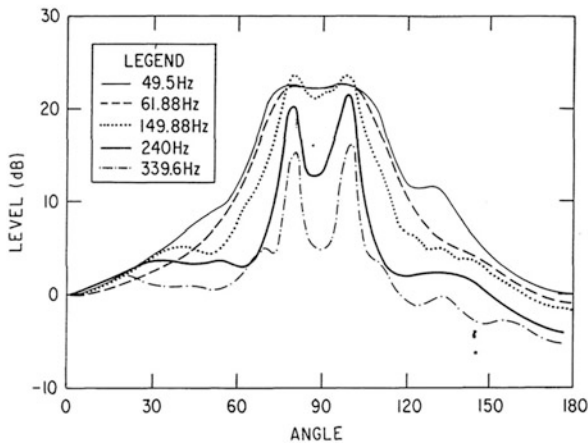

Fig. 4.22 Noise level versus vertical angle (0° is up, low sea state) taken from Fig. 4.18 at specific frequencies. The broad maximum along the horizontal at 49.5, 61.88, and 149.88 Hz is compared with the peaked distributions at 240 and 339 Hz

Figs. 4.21 and 4.22, measurements of the vertical noise directionality with an array in the sound channel (Fig. 4.19) have at the lower frequencies a broad pedestal centered on the horizontal direction, whereas at higher frequencies the pattern is peaked at the sound SOFAR angles. For an array at a different depth, the directionality, of course, will change with the arrival structure. For example, if the array were at the critical depth, a different directional pattern would be observed at all frequencies. An approximate ray angle analysis of the vertical directionality provides insight as to the variation of vertical directionality with depth. Sources of sound near the surface of the sea are dipolelike; consequently, the radiation pattern is directed downward and especially at higher frequencies is attenuated by multiple bottom interactions, thermocline variations in the sound speed, and rough surfaces interactions.

The measured results shown in Figs. 4.21 and 4.22 (Carey and Wagstaff 1986) were obtained by Anderson et al. (1972) with the maximum likelihood method of Edelblute et al. (1966) using a 26-element array in the Sargasso Sea south of

Bermuda. The array center was at a depth of 236 m in the sound channel with an axis depth of 1 km and was processed with a frequency resolution of 1.4 Hz.

Figure 4.21 shows the low-frequency plateau that begins to reduce in level at frequencies higher than 150 Hz to a "notch" (10 dB) along the horizontal (also see Fig. 4.22). The noise intensity at 150 Hz has a maximum at $90 \pm 9.5°$, compared with $90 \pm 14°$ if the array had been centered on the sound channel axis. A reference sound source at some distance on the axis is observed near 400 Hz. The results also show evidence of aliasing at frequencies greater than 400 Hz.

Since surface spectra are tonal in the low-frequency range, one would expect more of a variation of the level with frequency along the horizontal. The smooth variation of this pedestal along the horizontal with frequency indicates that broad-band, wind-induced sound in addition to ship-radiated noise may be important. Any source over the basin shelves, slopes, and seamounts will reflect sound into the channel, as the calculations using monopole sources a small distance below the surface show in Fig. 4.23. The calculations ignore local surface noise sources in the array vicinity but have a distribution in range of random noise sources with source levels based on a 10-knot wind speed. The calculated mid-basin omnidirectional noise levels of 65 dB at 50 Hz, 53 dB at 200 Hz, and 45 dB at 400 Hz were consistent with measured levels when only wind-induced noise is the source of sound. The 1974 measurements of Garabed and Finkelman (2005) and later measurements of Wales and Diachok (1981) in the Northwest Atlantic show this vertical directionality of the noise.
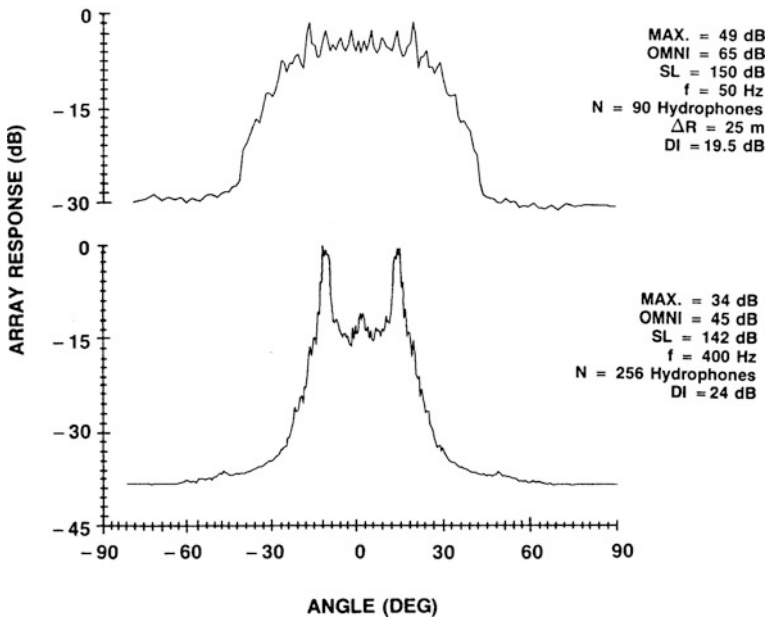

Fig. 4.23 Relative noise levels versus angle (+90° is up) for 50 and 400 Hz for the geometry and noise source distribution shown in Fig. 4.19

Since range-dependent sound velocity profiles, boundary reflections, and sound channel scattering couple energy from higher to lower angles and produce frequency-dependent losses, the combination of these effects was thought to be the primary cause of the vertical directivity characteristic. Although all are important, it appears that the first-order explanation is the downslope conversion of noise sources over the slopes and seamounts. The range-dependent environment in Fig. 4.19 was employed to numerically investigate these effects and a sample result is shown in Fig. 4.23. The sources were placed at a reference depth to ensure there were dipole or doublet characteristics and a scaled source level per unit area consistent with measurements of wind noise. The low frequency (50-Hz) sound is reflected from the slope with little loss and has a broad pedestal centered along the horizontal, whereas the higher frequency (400 Hz) with large loss produces a minimum along the horizontal. Using the same numerical method, the decrease in the sound channel toward the northern latitudes was examined and found to produce a smaller effect. The depth of the noise notch is shallow at higher frequencies owing to sound channel scattering from the thermocline and bathymetry changes. An interesting characteristic of Fig. 4.21 is the smooth frequency characteristic along the horizontal for frequencies less than 140 Hz.

Coincident measurements of the horizontal and vertical noise characteristics showed that when the horizontal directionality was successfully modeled only using surface-ship-radiated noise, the level of the horizontally directed noise and the subsequent pedestal in the vertical noise level distribution were underpredicted.

The experiments conducted by Wagstaff (2005) and Anderson (1979) featured the measurement of ship density and traffic using airborne observations, the measurement of horizontal directionality with high-resolution arrays, and the measurement of vertical noise directionality with an array that spanned the sound channel. The comparison of the measurements of the persistent directionality and the calculated directionality using the range-dependent bathymetry, sound speed structure and observed density of ships is shown in Fig. 4.24. Moderate agreement was found and is rather remarkable when one considers the estimated bottom reflectivity and source levels of the shipping. The comparison of the calculated and measured vertical directionality is shown in Fig. 4.25. Observe that the noise levels along the horizontal are higher for the measurements. This difference in the relative levels as a function of the angle from the horizontal indicates the calculations do not include all the noise sources over the shelf, such as wind-generated noise. This frequency-dependent characteristic also depends on the not well known slope reflectivity.

Nevertheless the downslope enhancement, megaphone effect, is an important factor.

Rain Noise

Many factors determine the radiated noise from rain. Certainly, the rate of rainfall, the state of the sea surface, and the presence of a subsurface bubble layer can be important with respect to the level and directional characteristic. The Wenz curve
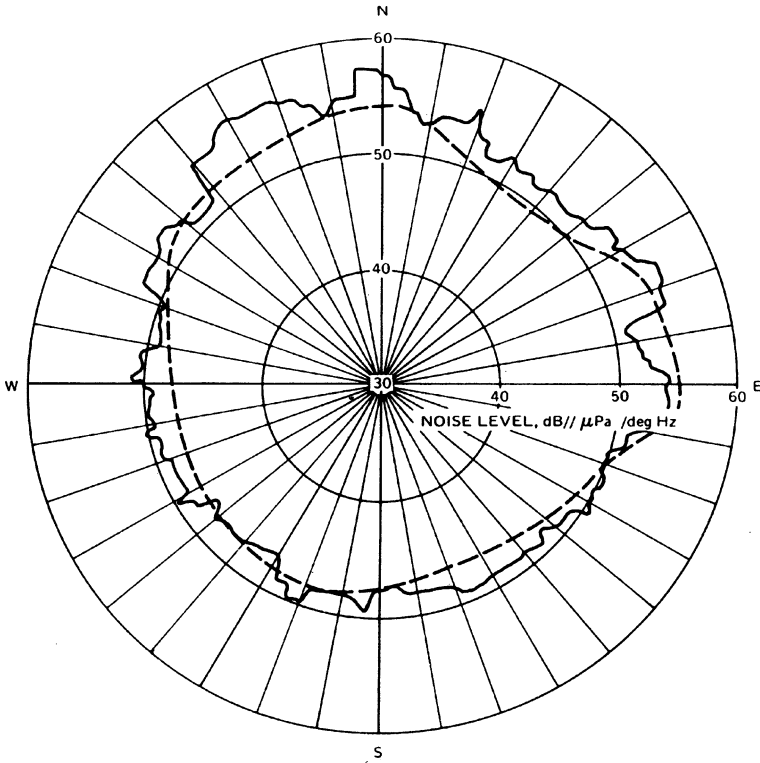
Fig. 4.24 Measured horizontal directionality in the Northeast Pacific Ocean (*solid curve*) compared with calculations based on range-dependent bathymetry, range-dependent sound velocity profiles, and measured density of ships. (Wagstaff 2005) and (Urick 1984)

presented in Fig. 4.2 shows the results from Heindsman et al. (1955) and represents the maximum noise levels measured during the passage of hurricane Edna. The sea state was 4 and the wind ranged from 20 to 40 knots. Heindsman et al. reported rainstorm measurements with a rainfall rate of 9 mm/h with a flat spectral characteristic from 0.1 to 20 kHz and a spectrum level of 80 *dB re* $((1\mu P_a)^2/Hz)$, equivalent to the levels measured by Knudsen et al. under similar conditions. The striking feature of the spectrum under the condition of heavy rains is its white spectral character. This characteristic was not generally observed for lighter rainfall rates, which produce a spectral peak in the 10–15-kHz region primarily due to oscillation of entrained bubbles. Fig. 4.26 shows the impact of a drop and an entrained bubble oscillation.

Franz (1959) (also see Fitzpatrick and Strasberg (1956, Fig. 18, p. 264)) performed a remarkable series of experiments of drops impinging on a liquid surface. His experiments were guided by the theoretical expectation based on a multipole expansion of a sound source at the free surface and the result that the radiated pressure would have the dipole radiation form:
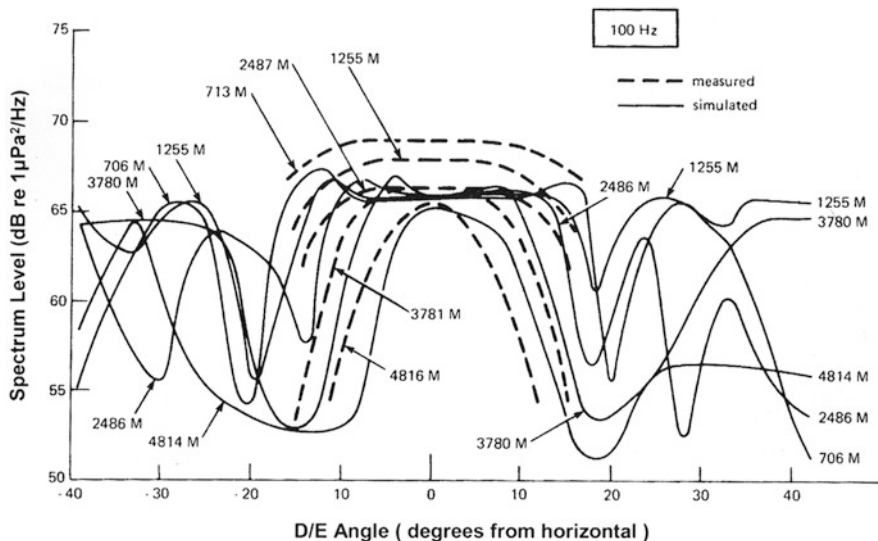
Fig. 4.25 Measured vertical noise directionality compared with calculations for the same case shown in Fig. 4.24 showing underprediction of the levels along the horizontal

$$p_s(r, \theta, t) = (\rho\, u^3 L_d\, cos(\theta)/rc)Z((u/L_d)(t - r/c)),\ L_d = 2a., \qquad (35)$$

where ρ is the density, u the impact speed, θ the polar angle, a the drop radius, and r the radial distance to the point of observation. Figure 4.26 shows one of the experimental sequences that identified two sources of sound, the impact and entrained bubble oscillation. Although a fairly white spectrum was observed, was the drop impact the dominant mechanism? Franz always observed the impact but not the bubble oscillation

The impact waveform and measured spectrum, shown in Fig. 4.27, interpreted with the above expression for the radiated pressure define the radiated sound of the impact. However, comparisons with measurements (Fig. 4.28) reveal that Franz's theoretical expectations produce levels less than observed by an order of 10 dB.

Guo and Ffowcs Williams (1991) reexamined the drop impact and determined that the cause of the radiated sound was the rapid momentum exchange between the drop and the water body. They applied the Kirchhoff integral theorem to develop an expression for the radiated pressure in terms of the vertical velocity at the pressure-release surface:

$$P(r, t) = (\rho_o/2\pi) \cdot \partial/\partial t \int_S \{u_3(y_x, \tau)/r\}dS_y. \qquad (36)$$

This is equivalent to one of the integral expressions (Eq. 21) developed in Chapter 3. They further showed that the supersonic contact circle was the cause of the short-duration compressive waves. As the contact circle becomes subsonic,
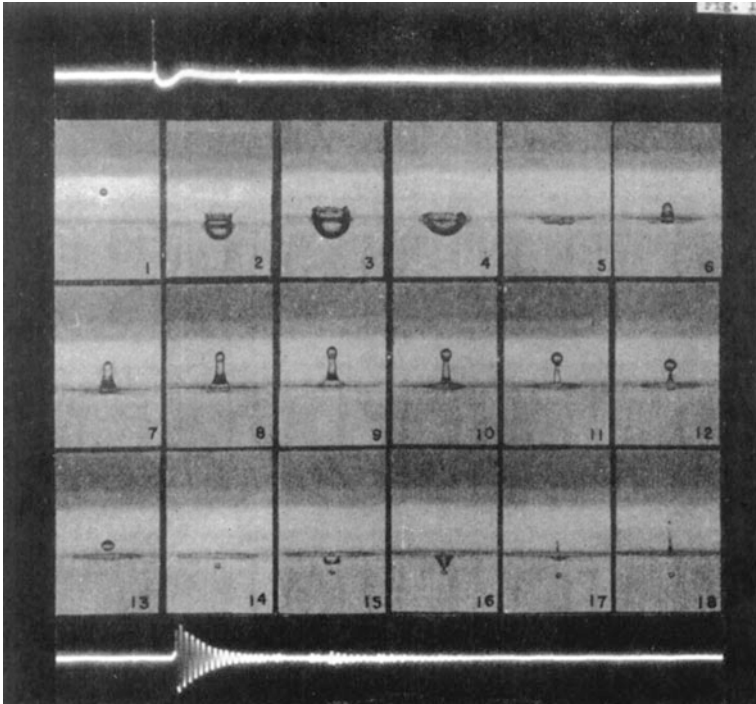
Fig. 4.26 The sequence of events of a liquid drop impinging on a water surface is shown by a series of photographs every 13 ms. Also shown is the corresponding oscilloscope trace of the impact (frames 1 and 2), the dampened sinusoid due to the bubble (frames 13 and 14), and the subsurface bubble frames (14–18). The radius of the droplet was 0.24 cm, the mass was 56 g, and the droplet speed was 350 cm/s. (Fitzpatrick and Strasberg 1956, Fig. 18)
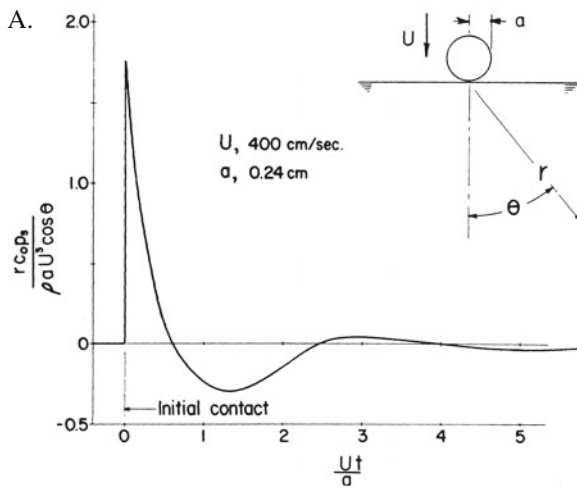

Fig. 4.27 The impact waveform (**a**) traced from an oscillograph record and the spectrum (**b**) are shown to characterize the sound produced by the vertical impact of water droplets
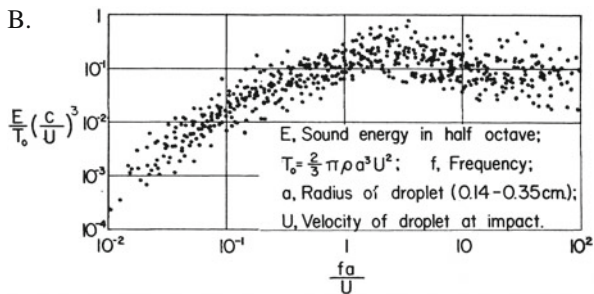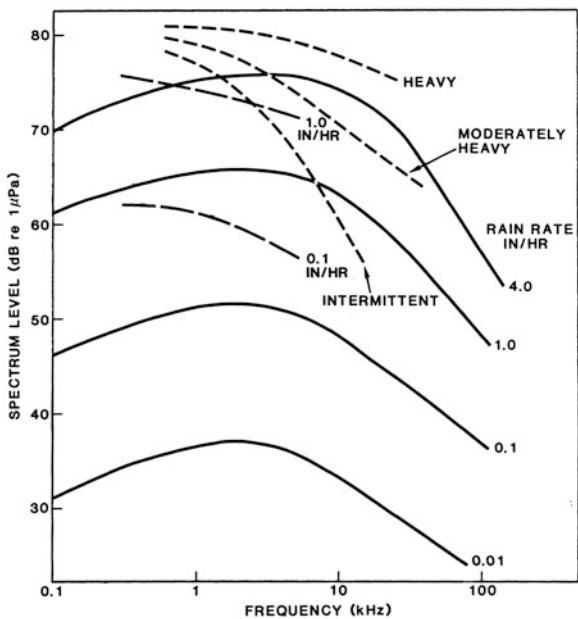
B.

Fig. 4.27   (continued)

Fig. 4.28   Measurements of the rainfall spectra by Heindsman et al. (1955) (*short dashes*) and Bom (1969) are shown in comparison with the theoretical estimates by Franz

the horizontally propagating wave has particle velocities greater than those of the contact circle expansion and, thus, disturbs the fluid ahead of the contact circle, reducing the relative velocity and, subsequently, the generation of additional sound. The result is a short-duration transient and slowly decaying tail. Since the initial impact is essentially a "water hammer," the initial pressure amplitude, p, is proportional to $\rho_o U c$; the subsequent three-dimensional propagation of the pulse reduces this amplitude. The radiated energy of the impact determines for a monodispersed distribution of drops the far-field intensity for a given rain rate:

$$R = (4\pi a^3/3)N, \quad N[\#/s]; \tag{37}$$

to be

$$I = (1/8)\rho_o U^2 \pi \, a^3 M^3 N = (3/32)\rho_o U^2 M^3 R. \tag{38}$$

If only the impact sound is important, the intensity of sound in moderate–heavy rain should be related linearly to the rainfall rate R. However, many factors change as the sea state increases, such as the surface roughening, waves breaking, and near-surface bubble layers.

The question addressed by Pumphrey and Crum (1989) and later by Pumphrey and Elmore (1990) was when are bubbles produced? Their answer, shown in Fig. 4.29, was that bubbles are produced by (1) irregular entrainment of bubbles caused by complex splashes, (2) regular entrainment caused by the crater resulting from drop impact and the formation of a smaller individual bubble, (3) entrainment of larger bubbles formed from the volume of the crater, and (4) Mesler entrainment of many small bubbles formed between capillary wave crests and at the instant of impact.

The importance of bubbles as sources of sound has been well established and if bubbles are produced by every impact, then their contribution to rain noise is beyond question. The simplified analysis of Franz ignored two important nondimensional
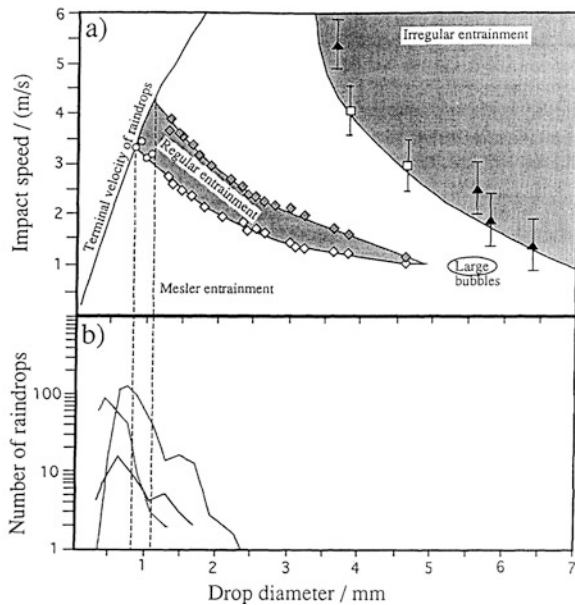

Fig. 4.29 **a** Rain drop impact speed versus the drop diameter for regions of irregular entrainment, regular entrainment, entrainment of larger bubbles, and Mesler entrainment. **b** The size distribution of rain drops, with the abscissa coincident with **a**

ratios: the Froude number, $Fr = U^2/L_d g$, and the Weber number, $We = \rho\, U^2 L_d/T$. These nondimensional ratios have a key bearing on bubble entrainment. Pumphrey and Elmore (1990) found that the boundary of the regular entrainment region (Fig. 4.29) corresponds to a relationship between these numbers as $Fr = A\, exp(BWe)$. In this expression A and B are constants, one pair for the highest drop speed and another for the lowest drop speeds that cause entrainment. Although this work is interesting, the fundamental characterization of the drop-entrainment process is not fully understood. Also shown in Fig. 4.29 is the bubble size range of 0.8–1.1 mm corresponding to normal-incidence drops at their terminal velocity impacting on the surface.

The radiation of a bubble near the surface can be described by (see Appendix G)

$$
\begin{aligned}
p_D &= ikD\cos(\theta)(1 + i/kr)\,exp(-\beta(t - r/c))\,exp(-i\omega_o t + ikr) \\
&\to ikD\cos(\theta)\,exp(-\beta(t - r/c))\,exp(-i\omega_o t + ikr)\,;
\end{aligned}
\tag{39}
$$

this equation describes a progressive dampened sine wave with frequency $f_o = 2\pi\omega_o$. The natural frequency of the bubble is given by the equation of Minnaert (1933) (see Appendix E),

$$
f_o = (1/a_o)\sqrt{3\gamma P_o/\rho}.
\tag{40}
$$

The spectral peak of the radiated noise from small bubbles is determined by the bubble size distribution and the dampening constant. This phenomenon reported by Nystuen for light rains has been widely observed. Notice as the wind speed increases in Fig. 4.30, the spectrum level decreases owing to the suppression of the regular entrainment of bubbles shown in Fig. 4.29
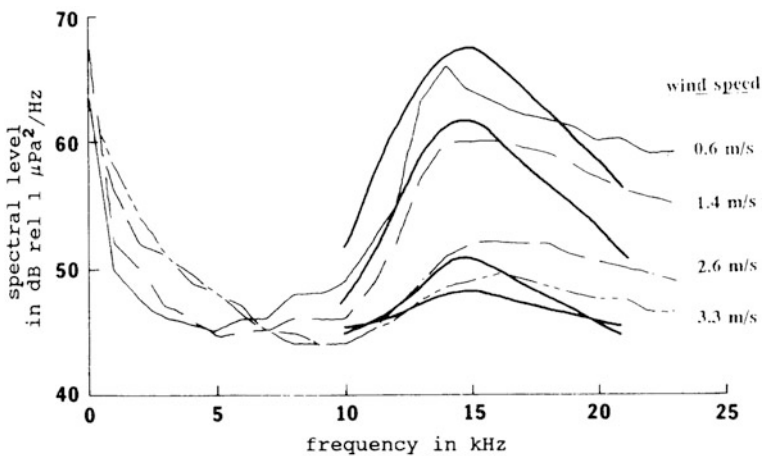

Fig. 4.30 The spectrum of light rain for various wind speeds (Nystuen 1993)

The spectral peak in the 12–15-kHz range corresponds to the regular entrainment of bubbles by drops at their terminal velocity. Also shown are Nystuen's prediction of the levels based on the drop size distributions of Pumphrey and Elmore (1990).

The rainfall sound intensity and spectrum characteristic can be described largely by the cumulative effects of many raindrop impacts that do not produce bubbles. However, when the rain is heavy, the broad spectral peak observed by Heindsman et al. in the region below 3 kHz requires another source such as the irregular entrainment of larger bubbles.

Arctic Ambient Noise

The Arctic Ocean can be considered to consist of four relatively distinct regions: the central Arctic, which is covered with pack ice; the coastal regions, which have shore-fast ice in the winter and a mixture during the summer; the marginal ice zone, which represents the progression from pack ice to an ice floe region; and, finally, the open waters, which are ice-free and adjacent to the marginal ice zone.

The central characteristic of the Arctic sound channel is the presence of ice and, consequently, it represents a unique noise environment. Noise is produced by the interaction of the pack ice and floes with the environmental forces such as the wind, rate of temperature change, radiation cooling, insolation, and mesoscale oceanic currents. These sources of sound are temporally variable as well as seasonal in nature. Because of this variability, the noise field can be up to 20 dB less than the level measured in the open ocean for a Knudsen sea state zero (Beaufort 1 in Fig. 2.2, Table 2.1) and up to levels corresponding to sea state 4 (Beaufort 5 in Fig. 2.2, Table 2.1). At low frequency, naturally occurring quakes, microseisms, ice cover standing and propagating surface waves, and water sediment boundary waves can all contribute to the noise field.

In addition to noise that originates from the ice, there is a rich source of both narrow-band and broadband noise from the soniferous marine fauna. During the summer, sounds such as long gliding whistles, short chirps, braying, groans, and grunts have been observed. However, biological noises in the Arctic are not dominant since the levels and duration are limited. On the other hand, during the summer in the Antarctic's McMurdo Sound, noise from seals and humpback whales dominates the spectrum from 200 to 800 Hz.

Finally, the Arctic noise field consists of man-made sounds from explosions, air guns, industrial activity, and icebreakers. These noise sources will not be treated even though their contributions to the ambient noise field can be at times significant.

Arctic Ambient Noise over the 10 Hz to 1 kHz Band

The interaction of the ice cover with the air and water boundary layer is the primary source of noise production. Since the ice covering has variable characteristics, such as brittleness, snow cover, thickness, surface roughness, and ridging, variability in

noise production is to be expected. Furthermore, the general forcing functions such as rate of temperature change, wind speed, oceanic currents, and tidal variations as well as the interaction with the ice are very complex. It is doubtful whether one could predict quantitatively the observed noise field; rather, it is the goal in this section to provide a qualitative understanding of the dominant observed characteristics.

Figure 4.31 shows the ambient noise results of Mellen and Marsh (1965). Curve A represents a quiet period over the frequency range of 10–1,000 Hz. The broad spectral peak observed around 30 Hz was thought to be due to distant sources. Curve B is representative of a cold period with a sudden change in temperature that produced thermal-stress-induced ice cracking. Curve C represents the highest noise levels observed.

These early observations of Arctic ambient noise are consistent with the work of Greene and Buck (1964), Milne and Ganton (1964), Milne (1965), and Ganton and Milne (1965). The basic cause of higher-frequency noise was considered in each work to be thermal-stress-induced cracking of the ice during cold periods with rapid decreases in temperature. By "cracking," one means a tensile opening and shear motion either toward the direction of or across the crack producing a series of slip–stick sounds. Surface cracks can be caused by radiation cooling and require a snow-free brittle ice. This effect is often observed in pack ice and shore-fast spring and winter ice. The ensemble of stick–slip emissions results in a short burst
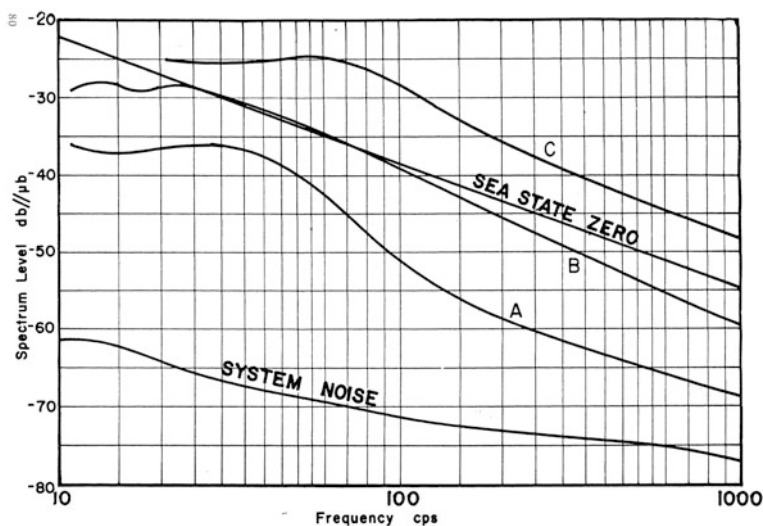
Fig. 4.31 Summary of ambient noise measurements from two ice islands made by Mellen and Marsh (1965). The ordinate is labeled "Spectrum level dB//μb." To convert to spectrum level dB re (μPa)^2/Hz simply add 100 to the ordinate. *Curve A* represents a typical quiet period. *Curve B* is representative of cold weather and a sudden decrease in air temperature. The rapid decline in air temperature causes the ice to become stressed and to crack. *Curve C* represents the highest levels observed

of sounds. These spiky and random slip–stick emissions, when not closely spaced in time, are decidedly non-Gaussian. However, when the number of transients per unit time produces a random waveform without identifiable individual events, the process becomes Gaussian.

Milne (1967) observed for the higher frequencies that two prime causes of noise were evident, wind speed and temperature change. To examine these causes he conducted experiments under similar ice conditions during the colder cooling periods with no solar radiation and during warming periods with variable winds, as shown in Fig. 4.32

During cooling trends, clear conditions and low (about $0\,m/s$) wind speed conditions, Milne observed te spectrum levels shown in Fig. 4.32a. Figure 4.32a shows the results for periods during which there was no wind but cooling, as shown by curves C, D, and E. Curve "A," labeled "residual impulsive noise," represents a limiting condition and was obtained under a period of warming with low (about $0\,m/s$) wind speed with levels 14 dB less than a sea state "0" condition. Also shown is a reference curve for noise levels with a 10-knot wind speed. The broad maximum
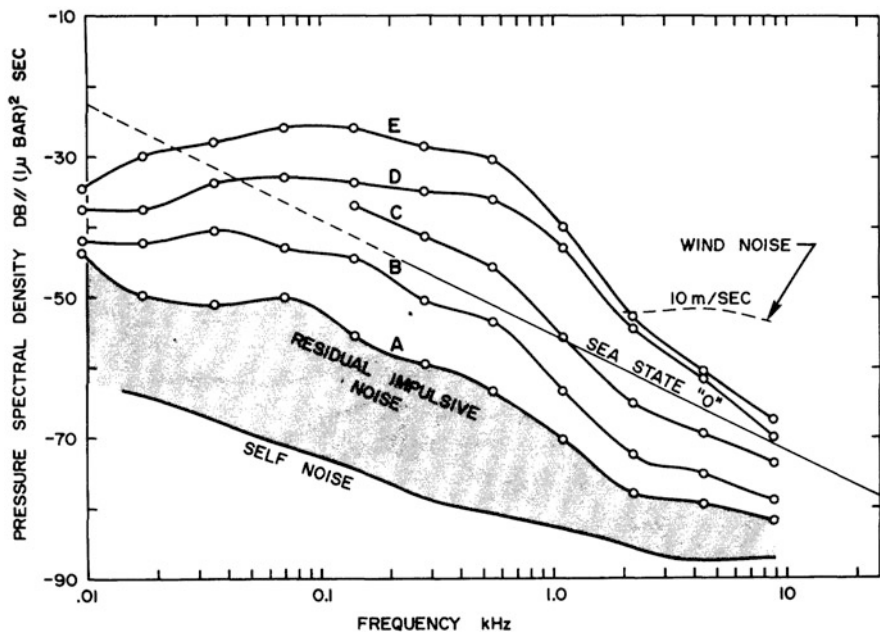
Fig. 4.32 Under ice pressure spectrum levels versus frequency during cooling with low (about $0\,m/s$) wind speed and under warming periods with increasing wind speed. The ordinate can be converted to $dB\,re\,(\mu\,Pa)^2/Hz$ by simply adding 100. (Milne 1967, Figs. 7.34 and 7.36). **a** Pressure spectrum level versus frequency of under ice noise measured during an air cooling period with low (about $0\,m/s$) wind speed illustrating ice cracking noise. **b** Pressure spectrum level versus frequency of under ice noise measured during an air warming period for various wind speeds

Fig. 4.32 (continued)

is in the 100–600-Hz range. Milne attributed the spectral characteristic of the noise during the cooling period to ice cracking, a large collection of impulsive events.
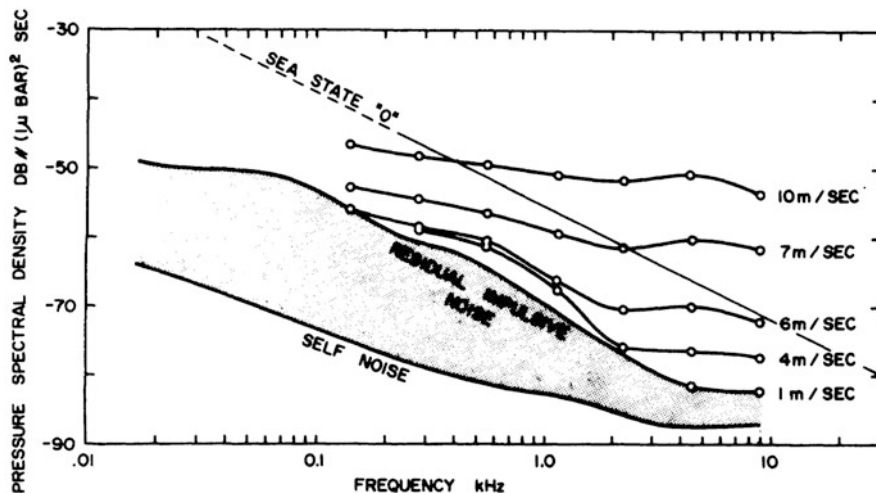
Shown in Fig. 4.32b is the case for air warming periods with variable wind speeds. Unlike the impulsive ice cracking noise, the observed wind speed noise had a whitened spectrum and a Gaussian amplitude distribution. This figure shows the noise levels for various wind speeds (measured at 5 m above the ice surface) as a function of frequency. The increase of the noise intensity is observed to be approximately proportional to the 5th power of the wind speed. The empirical equation developed by Milne is

$$<p^2> = v^{5.3} \times (1.6 \; 10^{-1}), \; [(\mu \, P_a)^2/Hz], \tag{41}$$

where the wind speed v is in meters per second.

The turbulent boundary layer can produce ice surface pressure fluctuation owing to the unevenness of the surface and, thus, can generate noise. However, this turbulent boundary layer can also cause snow pelting. That is, wind flow over the ice can produce miniature eddies of small snow and ice crystals that collapse in the lee to produce blowing snow, sounding very much as if the ice surface were being blasted with many small particles (Mellen and Marsh 1965). These sounds were found to have a Gaussian amplitude distribution. Milne and Ganton (1964) also observed that snow pellets can be lifted from the surface by flow eddies and subsequently impacted on the surface. For wind speeds greater than 4 m/s and for frequencies greater than 2 kHz, this wind speed noise can dominate. As one proceeds to lower frequencies, longer-range or distantly generated events are observed. Wind-induced noise should be seasonal and primarily a winter phenomenon. During the summer months, stable temperature and wind conditions result in quiet ambient noise levels

since broken ice is a poor noise maker as the slow jostling of floes does not much produce significant noise.

Low-Frequency Arctic Ambient Noise

An interesting phenomenon has been observed in the marginal ice zone: the dramatic increase in noise as one approaches the ice edge (Diachok and Winokur 1974). The results from Yang et al. (1987) shown in Fig. 4.33 were obtained in July over a 2 h period under sea state 2 conditions by use of air-dropped sonobuoys into the open water and polynas, which are water openings in the ice field. The nominal spacing was 28 km and the depth was 30 m. Measurements were made over a frequency range from 100 to 1,000 Hz. A sharp increase in noise at the compact ice edge was observed across the whole 100–1,000-Hz band and Fig. 4.33 shows the effect for a one-third-octave band centered at 315 Hz. The compact ice edge corresponds to ice concentration changes of one eighth to seven eighths of the area covered over a range of 1–2 km.

Also shown in Fig. 4.33 are the results from measurements made during April in the vicinity of a diffuse ice–water boundary corresponding to ice concentration changes of one eighth to seven eighths of the area covered over a range of 100 km. The spatial variation of the observed noise levels in the band centered on 315 Hz was
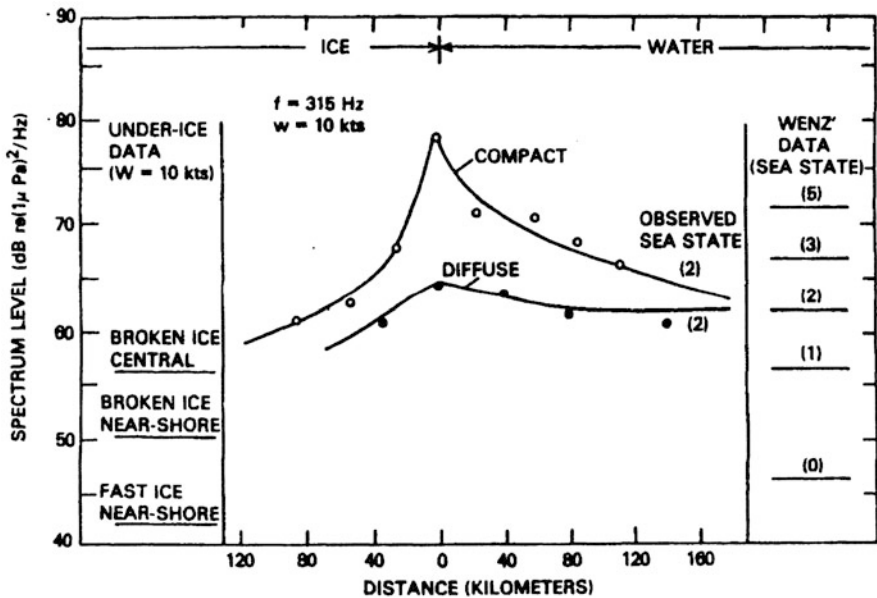

Fig. 4.33 Ambient noise results obtained in the Greenland Sea near the boundary of compact and diffuse ice floes and the open ocean. Also shown are the average noise levels under the ice-free and ice-covered regions. (Yang et al. 1987)

found to be more spatially uniform with a less pronounced increase in noise level near the edge. These results are consistent with those from other Arctic marginal ice zone investigations (Urick 1984, pp. 8-12 –8-14).

The result from all these investigations was that the ice edge acts as a distributor of sound producing higher noise levels on the open-ocean side of the zone and lower levels under the ice, with a broad maximum along the ice edge. This distribution of sound radiators along the edge was not in general uniform. Directional arrays towed at depth in the open-ocean areas parallel to the ice edge showed that regions of intense noise activity were observed and persisted for days.

The bumping and crashing of ice floes produced intermittent strong transients in the 100–1,000-Hz frequency band. The ice crush spectra were similar to those of thermal cracking and ice breaking. Since ice edge noise increased with wind speed and the density of floes, the combined role of wind, waves, and currents cannot be understated.

At very low frequencies, standing waves and flexural waves can occur on individual ice floes that may produce low-level pressure oscillation independent of depth at twice the frequency of gravity waves and the bobbing motion of ice floes:

$$Period\ T = 2(h\rho/g\rho_w)^{1/2},\ \ h = ice\ thickness = 2 - 3m,\ \ f_b = 0.35 - .7\,Hz \quad (42)$$

Figure 4.34 shows an interesting composite of low-frequency ambient noise results compiled by Dyer (1983). Each portion of the spectrum was obtained at
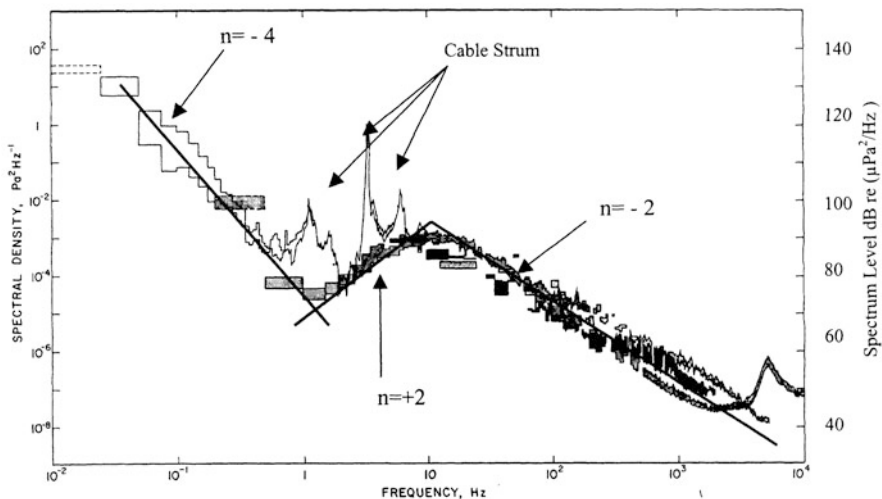

Fig. 4.34 Composite noise results from multiple sample periods under pack ice (83° N, 20° E, 1982) are shown to illustrate low-frequency noise characteristics. Also shown are the frequency dependencies of the spectral levels, $(f/f_{ref})^n$, and identified spectral features due to strum. [Adapted from Dyer (1983, Fig. 7, p. 24)]

different periods and placed in the composite to enable discussion of the basic noise characteristic and causative physical source mechanisms.

In the low frequency of the spectrum, 0.01–0.5 Hz, the spectrum decreases with approximately the fourth power of the frequency, n = −4, and Dyer considered this noise to be the result of hydrodynamic flow, subsurface oceanic currents, around the hydrophone and cable. He identified the spectral features caused by the flow-induced strum of the suspension cable coupled to the hydrophone.

A striking spectral feature was the broad low-frequency spectral peak near 10 Hz between 1 and 100 Hz, with frequency to the n = +2 power prior to the peak followed by frequency to the n = −2 power. This characteristic was found to be a regular feature of pack-ice noise. The region between 150 and 5,000 Hz was similar to the results of Milne discussed previously due to thermal cracking of the ice in periods of rapid cooling. Another peak was observed near 5,000 Hz during periods of high winds, most probably due to snow pelting.

Shepard (1979) concluded that the cause of the low-frequency spectral feature was a superposition of a short burst of sound; see Fig. 4.35. Even though the individual event may have a narrow steeper-sloped spectrum, the superposition of many such impulses would result in the spectral characteristic observed.

The "Arctic song" of Dyer, the broadly peaked spectrum from 1 to 100 Hz with a central peak in the 10-Hz band, was attributed to cracking and breaking of the pack ice. Ice, like many crystalline and regular granular materials, when under stress can crack and break. The acoustic emissions from such events are caused by stick and slip action of the breaking or cracking motion. Generally speaking, the emissions from many such events yield a lower-frequency, longer-duration acoustic emission. This phenomenon occurs from the seismic to ultrasonic scales. The resulting waves generated then propagate and are filtered by the response of the transmission path. Dyer (1984, pp. 13–15) provided an analytical treatment of this process by assuming that the shear displacement radiated from a small slip region in an infinite medium can be represented by a Gaussian proportional to the area-averaged slip displacement and the derivative of the time-dependent slip moment, $\dot{M}(t - r/c_s)$, with a retarded potential. The pressure radiated into the water requires the treatment of the ice–water interface. The traction across this interface introduces another time derivative of this moment due to the retarded time. Finally, another time derivative results from the ice–air boundary. Dyer concluded the pressure observed in the water is

$$P(r, t) = H(r)\,\dddot{M}(t - r/c_s) \tag{43}$$

where H is the total transfer function and c_s is the shear wave speed. This treatment, however, yielded the result shown in Fig. 4.35 with spectral slopes different from those observed.

Milne (1965) performed analysis of acoustic emissions from the ice. He assumed that the individual events were dampened sinusoids with random amplitudes, frequencies, locations, and time of occurrences. He derived the spectral characteristic
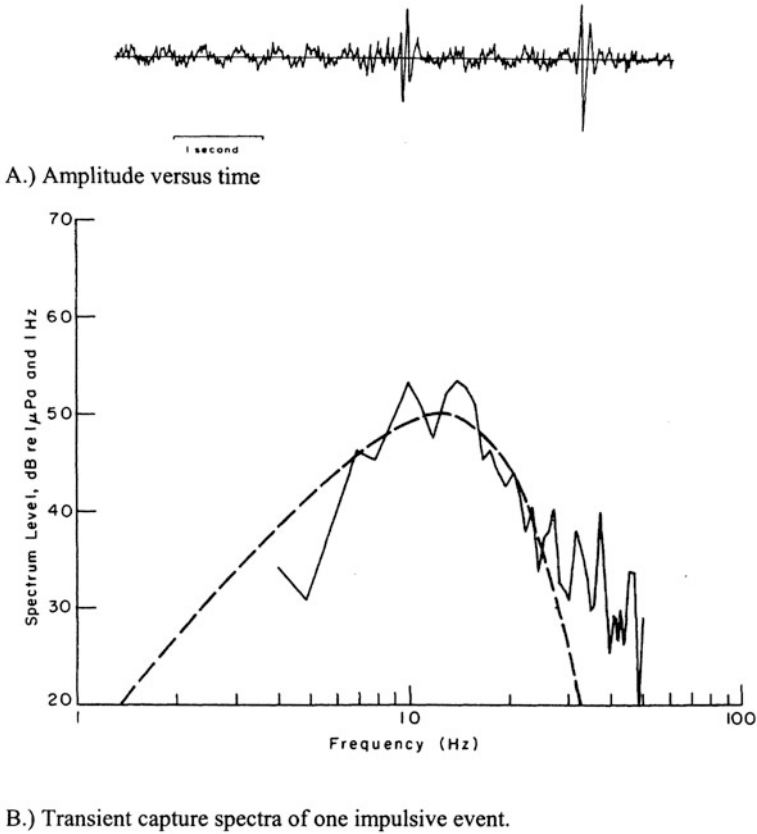
A.) Amplitude versus time

B.) Transient capture spectra of one impulsive event.

Fig. 4.35 The spectral characteristic of impulsive pressure pulses caused by stick–slip phenomena at the low frequencies that are generated by composite moments and stress due to environmental factors (Dyer 1983, Fig. 10)

using characteristic functions to show that at higher frequencies the spectral decline goes as n = −2. A similar analysis could be done on a collection of Gaussian pulses.

Since the measured acoustic pressure should be proportional to the third derivative of the slip displacement, noise is created when the ice fractures. The fracture or breaking of the ice is caused by the net stress and moments on the pack-ice sheet. Makris and Dyer (1986) chose as variables the composite ice stress, S, and composite ice moment, M, determined from the wind, current, cooling, and drift measurements. At low frequency, they concluded that only the wind current and drift were important. This conclusion was based on the temporal variation of the smoothed root mean square pressure in the 10–20-Hz band and its correlation with the temporal variations of the interrelated environmental variables, the effective stress S and moment M. The moment M and the stress S were found to provide the best correlation.

The Arctic sound channel may be an excellent tool for the observation of earthquakes owing to its low noise levels at frequencies less than 15 Hz and its excellent

sound transmission characteristic. The Mid Arctic Ridge (83° N, 5° W to 81° N, 120° E) is an active rift zone where earthquakes frequently occur. Keenan and Dyer (1984) observed the stick–slip radiation from these events. The durations can be as long as 100 s and must result from a sequence of emissions. The earthquakes radiate earthborn primary (compressional), secondary (shear) and tertiary waves. The energetic tertiary waves (400 kJ) enter the Arctic sound channels at steep angles and are converted to lower angles by the scattering from the meter-thick ice canopy. The fraction of acoustic energy is large, and durations of 72 s and tertiary wave waterborne arrivals have been observed 300 km from the source in the 5–15-Hz region [see Keenan and Dyer (1984, Fig. 7, p. 823)].

The mathematical description of stick–slip phenomena in the Arctic would seem to be a challenge as one could study earthquakes, ice quakes, microcracking, and a variety of other transient noise sources.

References and Suggested Readings

Introduction

Berlincourt, B. (1981). "Piezoelectric ceramics: Characteristics and applications." J. Acoust. Soc. Am. 70(6): 1586–1595.

Goodmann, R. (2004). A brief history of underwater acoustics in ASA at 75. Acoustical Society of America, Melville, New York, NY: pp. 204–227.

Knudsen, V. O., R. S. Alford, et al. (1948). "Underwater ambient noise." J. Marine Res. 7: 410–429.

Mason, W. P. (1981). "Piezoelectricity, its history and its applications." J. Acoust. Soc. Am. 70(6): 1561–1566.

Spitzer, L. (1945). *Physics of Sound in the Sea*. Peninsula Publishing, Los Altos, CA (1981).

Urick, R. J. (1984). *Ambient Noise in the Sea*. Undersea Warfare Technology Office, NAVSEA, D.O.N., Washington, DC (Also available from Peninsula Publishing, Los Altos, CA, 1986).

Wenz, G. (1962). "Acoustic ambient noise in the ocean: Spectra and sources." J. Acoust. Soc. Am. 34(12): 1936–1956.

Noise Measurement

Bendat, J. S. and A. G. Piersol (1966). *Measurement and Analysis of Random Data*. John Wiley & Sons, New York, NY.

Dyer, I. (1970). "Statistics of sound propagation in the ocean." J. Acoust. Soc. Am. 48(1, pt 2): 337–345.

Horton, C. W. (1968). *Signal Processing of Underwater Acoustic Waves*. U.S. Government Printing Office, Washington, DC (LOCC No.: 74-603409).

Middleton, D. (1987). *An Introduction to Statistical Communication Theory*. Peninsula Publishing, Los Altos, CA.

Pierce, A. D. (1981). *Acoustics: An Introduction to its Physical Principles and Applications*. Acoustical Society of America, Woodbury, NY.

Whalen, A. D. (1971). *Detection of Signals in Noise*. Academic Press, New York, NY.

Infrasonic Noise

Brekhovskikh, L. M. (1967). "Generation of sound waves in a liquid by surface waves." Sov. Phys. Acoust. 12(3): 323–350.

Cato, D. H. (1991a). "Sound generation in the vicinity of the sea surface: Source mechanisms and coupling to the received sound field." J. Acoust. Soc. Am. 89(3): 1076–1095.

Cato, D. H. (1991b). "Theoretical and measured underwater noise from surface orbital wave motion." J. Acoust. Soc. Am. 89(3): 1096–1112.

Goncharov, V. V. (1970). "Sound generation in the ocean by the interaction of surface waves and turbulence." Izv., Atmos. Ocean. Phys. 6(11): 1189–1196.

Hughes, B. (1976). "Estimates of underwater sound (and infrasound) produced by nonlinearly interacting ocean waves." J. Acoust. Soc. Am. 60(5): 1032–1039.

Isakovich, M. A. and B. F. Kur'yanov (1970). "Theory of low frequency noise in the ocean." Sov. Phys. Acoust. 16(1): 49–58.

Kibblewhite, A. C. and K. C. Ewans (1985). "Wave-wave interactions, microseisms, and infrasonic ambient noise in the ocean." J. Acoust. Soc. Am. 78(3): 981–994.

Kibblewhite, A. C. and C. Y. Wu (1989a). "The generation of infrasonic ambient noise in the ocean by nonlinear interaction of ocean surfaces waves." J . Acoust. Soc. Am. 85: 1935.

Kibblewhite, A. C. and C. Y. Wu (1989b). "A reexamination of the role of wave-wave interaction in ocean noise generation." J . Acoust. Soc. Am. 85: 1946.

Latham, G. V. and A. A. Nowroozi (1968). "Waves, weather, and ocean bottom microseisms." J. Geo. Res. 73(12): 3945–3956.

Lloyd, S. P. (1981). "Underwater sound from surface waves according to the Lighthill-Ribner Theory." J. Acoust. Soc. Am. 69(2): 425–435.

Longuet, M. S. (1950). "A theory of the origins of microseisms." Trans. Roy. Soc. A 243: 1–35.

Nichols, R. H. (1981). "Infrasonic ambient noise measurements: Eleuthera." J. Acoust. Soc. Am. 69(4): 974–981.

Urick, R. J. (1984). *Ambient Noise in the Sea*. U.S.G.P.O., Washington, DC (Peninsula Publishing, Los Altos, CA (1986)), pp. 456–963.

Wilson, J. H. (1979). "Very low frequency (VLF) wind-generated noise produced by turbulent pressure fluctuations in the atmosphere near the ocean surface." J. Acoust. Soc. Am. 66(5): 1499–1507 [Cato, D. H. (1981) "Comments on......." J. Acoust. Soc. Am. 70(6): 1783–1784 and Wilson, J. H. (1981) "Rebuttal to......" J. Acoust. Soc. Am. 70(6): 1785–1786.].

Phenomenological Observations of Ambient Noise

Anderson, D. et al. (1972). VLAM Data Analysis-Site 3, Bermuda, Naval Ocean Systems Center, San Diego, CA.

Anderson, V. C. (1979). "Variation of the vertical directionality of noise with depth in the North Pacific." J. Acoust. Soc. Am. 66: 1446–1452.

Arase, E. M. and T. Arase (1965). "Correlation of ambient sea noise." J. Acoust. Soc. Am. 40(1): 205–210.

Axelrod, E., B. Schoomer, et al. (1965). "Vertical directionality of ambient noise in the deep ocean of a site near Bermuda." J. Acoust. Soc. Am. 36(11): 77–83.

Bannister, R. W. (1986). "Deep sound channel noise from high-latitude winds." J. Acoust. Soc. Am. 79(1): 41–48.

Bannister, R. W., R. N. Denham, et al. (1981). Measurement of the Low-Frequency Wind-Generated Ambient Noise in the Deep Ocean, Naval Underwater Systems Center, TD 6565 (Available DTIC A65005).

Buckingham, M. and J. Potter (1995). *Sea Surface Sound'94*. World Scientific, Singapore, 1995.

Burgess, A. S. and Kewley, D. J. (1983). "Wind-generated surface noise source levels in deep water east of Australia." J. Acoust. Soc. Am. 73(1): 201–210.

Carey, W. M. and D. G. Browning (1988). Low-frequency ocean ambient noise, measurement and theory. *Sea Surface Sound*. B. R. Kerman (Ed.), Kluwer Press, Boston, MA, pp. 361–376.

Carey, W. M., R. B. Evans, et al. (1990). "Deep-ocean noise directionality." IEEE J. Ocean. Eng. 15: 324–334.

Carey, W. M. and E. C. Monahan (1990). "Guest Editorial "Special Issue" on sea surface-generated ambient noise: 20-2000 Hz." IEEE J. Ocean. Eng. 15(4): 265–266.

Carey, W. M. and R. A. Wagstaff (1986). "Low-frequency noise fields." J. Acoust. Soc. Am. 80(5): 1523–1526.

Cato, D. H. (1976). "Ambient sea noise in waters near Australia." J. Acoust. Soc. Am. 60(2): 320–328.

Chapman, N. R. and J. W. Cornish (1993). "Wind dependence of deep ocean ambient noise at low frequencies." J. Acoust. Soc. Am. 98: 782–789.

Cox, H. (1973). "Spatial correlation in arbitrary noise fields with application to ambient sea noise." J. Acoust. Soc. Am. 54(5): 1289–1301.

Cron, B. F., B. C. Hassell, et al. (1965). "Comparison of theoretical and experimental values of spatial correlation." J. Acoust. Soc. Am. 37(3): 523–529.

Cron, B. F. and C. H. Sherman (1962). "Spatial-correlation functions for various noise models." J. Acoust. Soc. Am. 34(11): 1732–1736.

Edelblute, D. J., J. M. Fisk, and G. L. Kinnison (1966). "Criteria for optimum signal-detection theory for arrays." J. Acoust. Soc. Am. 41: 199–205.

Fox, G. E. (1964). "Ambient-noise directivity measurements." J. Acoust. Soc. Am. 36: 1537–1540.

Franz, G. J. (1959). "Splashes as sources of sounds in liquids." J. Acoust. Soc. Am. 31(8): 1080–1096.

Furduev, A. V. (1966). "Undersurface cavitation as a source of noise in the ocean." Atmos. Ocean. Phys. 2(235): 314–320.

Garabed, E. P. and R. A. Finkelman (2005). "Measured vertical noise directionality at five sites in the western North Atlantic." IEEE J. Ocean. Eng. 30(2) (Special Issue, Archival Papers): 282–285.

Hollett, R. D. (1992). Observation of Underwater Sound at Frequencies Below 1500 Hz from Breaking Waves at Sea SACLANTCEN Rpt. 183, SACLANT Undersea Research Centre, 19138 San Bartolomeo, Italy.

Hollinberger, D. E. and D. W. Bruder (1990). "Ambient noise data Logger Buoy." IEEE J. Ocean. Eng. 15(4): 286–291.

Kennedy, R. and T. Goodnow (1990). "Measuring the vertical directional spectra caused by sea surface sound." IEEE J. Ocean. Eng. 15(4).

Kerman, B. R. (1984). "Underwater sound generation by breaking waves." J. Acoust. Soc. Am. 75(1): 149–165.

Kerman, B. R. (1988). *Sea Surface Sound*. Kluwer Academic Publishers, Boston, MA.

Kerman, B. R. (1993). *Natural Physical Sources of Underwater Sound*. Kluwer, Dordrecht, The Netherlands.

Kibblewhite, A. C. (1984). "Attenuation of low frequency sound in the sea, Vol. II." J . Acoust. Soc. Am. 75: 645.

Kibblewhite, A. C. and K. C. Ewans (1985). "Wave-wave interactions, microseisms, and infrasonic ambient noise in the ocean." J. Acoust. Soc. Am. 78(3): 981–994.

Kibblewhite, A. C., J. A. Shooter, et al. (1976). "Examination of attenuation at very low frequencies using deep water ambient noise field." J. Acoust. Soc. Am. 60: 1040.

Kibblewhite, A. C. and C. Y. Wu (1989a). "The generation of infrasonic ambient noise in the ocean by nonlinear interaction of ocean surfaces waves." J . Acoust. Soc. Am. 85: 1935.

Kibblewhite, A. C. and C. Y. Wu (1989b). "A reexamination of the role of wave–wave interaction in ocean noise generation." J . Acoust. Soc. Am. 85: 1946.

Knudsen, V. O., R. S. Alford, et al. (1948). "Underwater ambient noise." J. Marine Res. 7: 410–429.

Nystuen, J. A. (1986). "Rainfall measurements using underwater ambient noise." J. Acoust. Soc. Am. 79(4): 972–982.

Perrone, A. (1969). "Deep-ocean ambient noise spectra in the Northeast Atlantic." J. Acoust. Soc. Am. 46(3): 762–770.

Perrone, A. (1976). Summary of a One Year Ambient Noise Measurement Program Off Bermuda, Naval Underwater Systems Center, New London Laboratory, NUSC T.R. 4979 (Available DTIC).

Piggott, C. L. (1964). "Ambient sea noise at low frequencies in the shallow water of the Scotian Shelf." J. Acoust. Soc. Am. 36(1): 2152–2163.

Shang, E. C. and V. C. Anderson (1986). "Surface-generated noise under low wind speed at Kilohertz frequencies." J. Acoust. Soc. Am. 79(4): 964–971.

Shooter, J., T. DeMary, et al. (1990). "Depth dependence noise resulting from ship traffic and wind." IEEE J. Ocean. Eng. 15(4): 292–298.

Shooter, J. and M. Gentry (1981). "Wind generated noise in the Pareca Vela Basin." J. Acoust. Soc. Am. 70(6): 1757–1761.

Talham, R. J. (1964). "Ambient-sea-noise model." J. Acoust. Soc. Am. 36: 1541–1544.

Urick, R. J. (1984). *Ambient Noise in the Sea*. U.S.G.P.O., Washington, DC (Peninsula Publishing, Los Altos, CA (1986)), pp. 456–963.

Wagstaff, R. A. (1978). "Interactive techniques for ambient noise horizontal directionality estimation from towed line-array data." J. Acoust. Soc. Am. 63: 863–869.

Wagstaff, R. A. (1981). "Low-frequency ambient noise in the deep sound channel – the missing component." J. Acoust. Soc. Am. 69: 1009–1014.

Wagstaff, R. A. (2005). "An ambient noise model for the Northeast Pacific Basin." IEEE J. Ocean. Eng. 30(2) (Special Issue Archival Papers): 245–247.

Wales, S. C. and O. I. Diachok (1981). "Ambient noise vertical directionality in the Northwest Atlantic." J. Acoust. Soc. Am. 70: 577–582.

Wenz, G. (1962). "Acoustic ambient noise in the ocean: Spectra and sources." J. Acoust. Soc. Am. 34(12): 1936–1956.

Wenz, G. M. (1972). "Review of underwater acoustics research: Noise." J. Acoust. Soc. Am. 51(2 pt 3): 1010–1024.

Wille, P. C. and D. Geyer (1984). "Measurements on the origin of wind dependent noise variability in shallow water." J . Acoust. Soc. Am. 71(4): 173–195.

Wittenborn, A. F. (1976). Ambient Noise and Associated Propagation Factors as a Function of Depth-Wind-Speed in the Deep Ocean, Tracor Rept. T76RV5060, DTIC (AD 006902), Alexandria, VA.

Worley, R. D. and R. A. Walker (1982). "Low-frequency ambient noise ans sound transmission over a thinly sedimented rock bottom." J. Acoust. Soc. Am. 71(4): 863–870.

Rain Noise

Bom, N. (1969). "Effect of rain on underwater noise level." J. Acoust. Soc. Am. 45(1): 150–156.

Fitzpatrick, H. M. and M. Strasberg (1956). Hydrodynamic Sources of Sound. In *Naval Hydrodynamics*. F. S. Sherman (Ed.), National Academy of Sciences-National Research Council Pub 515, LC-57-60045, pp. 241–280.

Franz, G. J. (1959). "Splashes as sources of sounds in liquids." J. Acoust. Soc. Am. 31(8): 1080–1096.

Guo, Y. P. and J. E. FFowcs-Williams (1991). "A theoretical study of drop impact sound and rain noise." J. Fluid Mech. 227: 345–355.

Heindsman, T. E., R. H. Smith, et al. (1955). "Effect of rain upon underwater noise levels." J. Acoust. Soc. Am. 27: 378–379.

Minnaert, M. (1933). "Musical air-bubbles and sounds of running water." Phil. Mag. XVI (7th Series): 235–249.

Nystuen, J. A. (1986). "Rainfall measurements using underwater ambient noise." J. Acoust. Soc. Am. 79(4): 972–982.

Nystuen, J. A. (1993). An explanation of the sound generated in light in the presence of wind. In *Natural Physical Sources of Underwater Sound*. B. R. Kerman (Ed.), Kluwer Academic Publishers, Boston, pp. 659–668.

Pumphrey, H. C. (1989). "Sources of Ambient Noise in the Ocean: An Experimental Investigation." University of Mississippi, University, MS [Dissertation (NCPA LC.01-1989, Available DTIC)].

Pumphrey, H. C. and L. A. Crum (1989). "Underwater sound produced by individual drop impacts and rainfall." J. Acoust. Soc. Am. 85: 1518–1526.

Pumphrey, H. C. and L. A. Crum (1990). "Free oscillations of near surface bubbles as sources of underwater rain noise." J. Acoust. Soc. Am. 87: 142.

Pumphrey, H. C. and P. A. Elmore (1990). "The entrainment of bubbles by drop impacts." J. Fluid Mech. 220: 539–567.

Arctic Noise

Diachok, O. I. and R. S. Winokur (1974). "Spatial variability of underwater ambient noise at the Arctic ice-water boundary." J. Acoust. Soc. Am. 56(4): 750–753.

Dyer, I. (1983). Song of sea ice and other Arctic ocean melodies. In *Arctic Technology and Policy*. I. Dyer and C. Chryssostomidis (Eds.), Hemisphere Publishing Corporation, New York, NY, pp. 11–37, ISBN 0-89116-361-1.

Dyer, I. and C. Chryssostomidis (1983). *Arctic Technology and Policy*. Hemisphere Publishing Corporation, New York, NY, ISBN 0-89116-361-1.

Ganton, J. H. and A. R. Milne (1965). "Temperature- and wind-dependent ambient noise under midwinter pack ice." J. Acoust. Soc. Am. 36: 406–411.

Greene, C. R. and B. B. Buck (1964). "Arctic ocean ambient noise." J. Acoust. Soc. Am. 36(6): 1218–1220.

Hunkins, K. (1962). "Waves on the Arctic ocean." J. Geophys. Res. 67: 2477–2489.

Keenan, R. E. and I. Dyer (1984). "Noise from Arctic earthquakes." J. Acoust. Soc. Am. 75(3): 819–825.

Macpherson, J. D. (1962). "Some under-ice acoustic ambient noise measurements." J. Acoust. Soc. Am. 34(8): 1149–1150.

Makris, N. C. and I. Dyer (1986). "Environmental correlates of pack ice noise." J. Acoust. Soc. Am. 79(5): 1434–1440.

Mellen, R. H. and H. W. Marsh (1965). Underwater sound in the Arctic ocean. In *Scientific and Engineering Studies: Underwater Acoustics in the Arctic, 1958–1984*. W. A. Von Winkle (Ed.), Naval Underwater Systems Center (Now the Naval Undersea Warfare Center) Newport, RI.

Milne, A. R. (1965). "Statistical description of noise under shore-fast sea ice in winter." J. Acoust. Soc. Am. 39(6): 1174–1182.

Milne, A. R. (1967). Sound propagation and ambient noise under sea ice. In *Underwater Acoustics, Vol. 2*. V. M. Albers (Ed.), Plenum Press, New York, NY, pp. 103–138.

Milne, A. R. and J. H. Ganton (1964). "Ambient noise under Arctic sea ice." J. Acoust. Soc. Am. 36(5): 855–863.

Shepard, G. W. (1979). Arctic ocean ambient noise. *Ocean Engineering*. Massachusetts Institute of Technology, Cambridge, MA.

Urick, R. J. (1984). *Ambient Noise in the Sea*. U.S.G.P.O., Washington, DC (Peninsula Publishing, Los Altos, CA(1986)), pp. 456–963.

VonWinkle, W. A. (1963). "Vertical directionality of deep-ocean noise." J . Acoust. Soc. Am. 35:
    1884.
Von Winkle, W. A. (Ed.) (1984). *Scientific and Engineering Studies: Underwater Acoustics in
    the Arctic, 1958–1984.* Naval Underwater Systems Center (Now the Naval Undersea Warfare
    Center) Newport, RI.
Yang, T. C., G. R. Giellis, et al. (1987). "Acoustic properties of ice edge noise in the Greenland
    sea." J. Acoust. Soc. Am. 82(3): 1034–1038.